

Testing Models of Triggered Star Formation with Young Stellar Objects in Cepheus OB4

ABBY MINTZ,^{1,2} JOSEPH L. HORA,² AND ELAINE WINSTON²

¹*Department of Astronomy, Yale University, 52 Hillhouse Ave., New Haven, CT 06511, USA*

²*Center for Astrophysics | Harvard & Smithsonian, 60 Garden St., MS-65, Cambridge MA 02138, USA*

ABSTRACT

OB associations are home to newly formed massive stars, whose turbulent winds and ionizing flux create H II regions rich with star formation. Studying the distribution and abundance of young stellar objects (YSOs) in these ionized bubbles can provide essential insight into the physical processes that shape their formation, allowing us to test competing models of star formation. In this work, we examined one such OB association, Cepheus OB4 (Cep OB4) – a well-suited region for studying YSOs due to its Galactic location, proximity, and geometry. We created a photometric catalog from *Spitzer*/IRAC mosaics in bands 1 (3.6 μm) and 2 (4.5 μm). We supplemented the catalog with photometry from *WISE*, 2MASS, IRAC bands 3 (5.8 μm) and 4 (8.0 μm), MIPS 24 μm , and MMIRS near IR data. We used color-color selections to identify 821 YSOs, which we classified using the IR slope of the YSOs’ spectral energy distributions (SEDs), finding 67 Class I, 103 flat spectrum, 569 Class II, and 82 Class III YSOs. We conducted a clustering analysis of the Cep OB4 YSOs and fit their SEDs. We found many young Class I objects distributed in the surrounding shell and pillars as well as a relative age gradient of unclustered sources, with YSOs generally decreasing in age with distance from the central cluster. Both of these results indicate that the expansion of the H II region may have triggered star formation in Cep OB4.

Keywords: Young stellar objects; Star formation; Star forming regions

1. INTRODUCTION

Many stars in our galaxy formed in OB associations, loose unbound systems of massive O and B stars (Briceño et al. 2007; Lada 1999). The environments of OB associations, typically embedded in giant molecular clouds (GMCs), are strongly affected by massive stars ($> 8 M_{\odot}$) whose turbulent and fast-paced lives dramatically shape their surroundings (Zinnecker & Yorke 2007). Such OB associations also host less massive star formation and therefore young, less massive stars. Massive stars are an integral part of galactic evolution, providing heavy metals, massive outflows, and turbulent winds that greatly influence their environments (Zinnecker & Yorke 2007). Despite their important role in shaping astrophysical conditions, the processes that lead to their formation are still not entirely understood. Directly observing O and B stars in the midst of formation

is difficult due to dust extinction, their relatively low numbers and greater distances, and the relative brevity of their formation period.

Observing their effects on less-massive stars’ presence and development in OB associations is more feasible, in part due to the creation of ionized H II regions and the longer life cycle of less-massive stars. The stellar winds and ionizing flux from massive stars form H II regions within GMCs, pushing material from inside the OB association to the outskirts of the H II regions. These ionized bubbles have borders of dense material, nebulous features, and filaments, all of which can be sites of lower-mass star formation. Many star-forming H II regions with bubble morphologies have been studied previously, including Sh2-236 (Ortega et al. 2020), Sh2-48 (Ortega et al. 2013), and Vela OB2 (Cantat-Gaudin et al. 2019) among others (Xu et al. 2014).

The presence, distribution, and location of YSOs provides information about recent star formation in the OB associations and can help determine what physical processes are at play. The collect and collapse model posits that winds and supernovae caused by massive

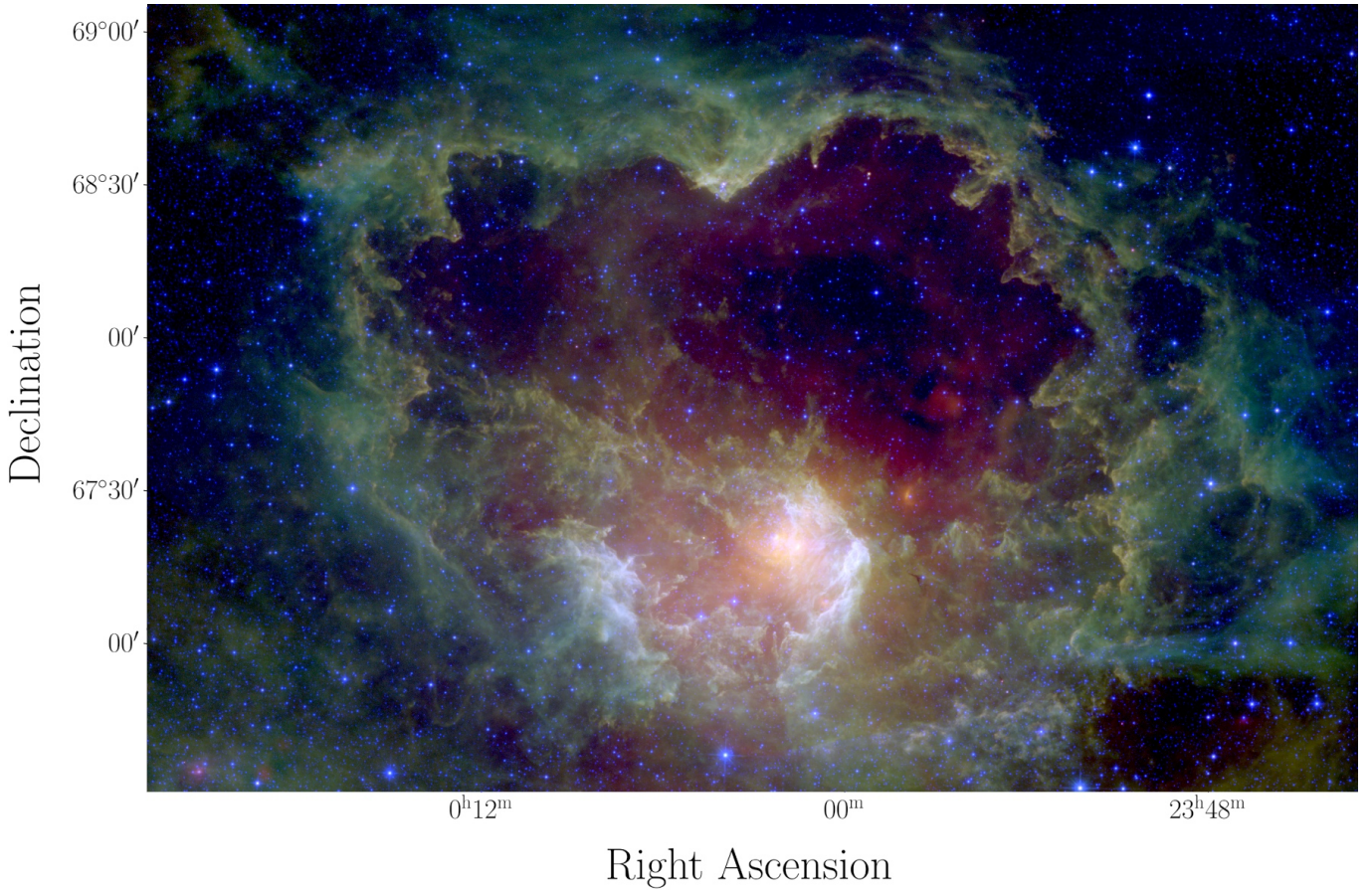


Figure 1. A color image of the Cep OB4 field using the *WISE* 3.4, 12, and 22 μm images (blue: 3.4 μm , green: 12 μm , red: 22 μm). Berkeley 59 – the cluster of early-type stars – can be seen in the southern central region of the image. The shell of the molecular cloud surrounds most of the bright stars in the image. Pillars around the edges of the shell point in towards the OB association.

stars can compress material sufficiently to trigger star formation by spurring gravitational collapse (Elmegreen & Lada 1977). This process would lead to the presence of YSOs around the outskirts of the H II regions, decreasing in age with increasing distance from the OB association’s center. A second model, radiation-driven implosion, suggests that star formation may result from the ionization front’s interaction with dense molecular regions, triggering increased density and collapse (Reipurth 1983). This model would yield clusters of YSOs in molecular structures like pillars that the H II region has expanded to include. A third proposed mechanism involves molecular cloud collisions (Loren 1976). YSOs would be formed in the dense regions created by the colliding material and would therefore be found in the areas of collision.

The OB association Cepheus OB4 (Cep OB4) is a potentially useful testing ground for star formation models due to its Galactic location, proximity, and geometry. Cep OB4 was first identified in 1959 along with an in-

terior cluster of early-type stars – Berkeley 59 (Be 59; Blanco & Williams 1959; Kun et al. 2008), which has been recently studied by Rosvick & Majaess (2013) and is estimated to be ~ 2 Myr old (Panwar et al. 2018). Several OB stars in the region have been cataloged, including some in the central Be 59 area (Skiff 2014). These massive stars are likely the source of the shockwave that evacuated the molecular material and created the bubble’s shape and structure. Cep OB4’s Galactic latitude of about $+5^\circ$ places it off of the densest area of the Galactic plane, which results in lower foreground and background contamination. At ~ 1.1 kpc (Kuhn et al. 2019) it is relatively close for an OB association, allowing for better resolution of individual sources and detection of lower-mass YSOs – down to a few tenths of a solar mass (Hora et al. 2018). With an estimated radius of 140 pc (Olano et al. 2006, adjusted to the 1.1 kpc distance), it is larger than the typical OB association where the average diameter has been estimated to be ~ 140 pc (Garmany 1994). Be 59 is also embedded in and ex-

panding into an approximately circular molecular cloud with a diameter of ~ 80 pc, allowing us to test models of sequential star formation.

In this work, we use new mosaics of the Cep OB4 OB association taken with the Infrared Array Camera (IRAC; Fazio et al. 2004a) on the *Spitzer Space Telescope* (Werner et al. 2004) to identify YSOs based on their excess IR emission (a result of the reprocessed stellar radiation in their surrounding dusty material). In Section 2 we describe the images and photometric catalogs used in our analysis. In Section 3, we perform photometry on the new images and cross match the resulting catalog with additional near and mid infrared photometry to extend our wavelength coverage.

In Section 4 we use the compiled photometric catalog to remove background sources, identify YSOs with various color-color selections, and classify the YSOs based on the slopes of their spectral energy distributions (SEDs). In Section 5 we study the spatial clustering and distribution of the YSOs, focusing especially on the youngest objects. In Section 6, we fit the YSO SEDs to determine their relative masses, which we used to construct the initial mass function for Cep OB4. In Section 7 we discuss our results, comparing our YSO analysis to various models of triggered star formation. We conclude with a summary of our findings in Section 8.

2. OBSERVATIONS

2.1. *Spitzer* IRAC

Cep OB4 was mapped by several *Spitzer* programs during the mission. The list of Astronomical Observation Requests (AORs) used to construct our mosaics is shown in Table 1. The programs prior to 2013 obtained individual pointings or small maps covering sources of special interest in the region. The programs conducted in 2003 and 2004 obtained images in all four IRAC bands (3.6, 4.5, 5.8, and 8 μm). The other programs were conducted during the *Spitzer* Warm Mission and therefore obtained data only in the 3.6 and 4.5 μm IRAC bands. Program 90179 mapped an approximately $1^\circ \times 1^\circ$ area covering the Be 59 cluster using 30 second HDR mode (1.2 and 30 second frames) with 5 dithers per map pointing. The majority of the mosaic was obtained in Program 14005 using 12 second HDR mode (0.6 and 12 second frames) and 3 dithers per pointing. Several AORs were necessary to map the full area.

We constructed the mosaic images using the corrected Basic Calibrated Data (cBCD) products produced by the *Spitzer* Science Center pipeline. In addition to the basic pipeline calibration and artifact correction, we constructed and subtracted residual background frames

Table 1. IRAC observations used in mosaics

AOR	Observation Date	Program	PI ^a
3658240	2003-12-23 13:33:58	6	Fazio
6034688	2004-07-28 16:01:13	202	Fazio
6034176	2004-07-28 16:06:27	202	Fazio
41713920	2011-01-28 08:46:17	70062	Kirkpatrick
44743424	2012-04-19 10:52:50	80109	Kirkpatrick
48001280	2013-04-12 10:27:38	90179	Getman
68418048	2018-11-17 11:04:31	14005	Hora
68418816	2018-11-17 12:12:22	14005	Hora
68418560	2018-11-17 14:25:05	14005	Hora
68419072	2018-11-18 04:07:57	14005	Hora
68418304	2018-11-19 09:37:45	14005	Hora
68516608	2019-01-04 06:17:35	14005	Hora
68515840	2019-01-04 07:24:52	14005	Hora
68516096	2019-01-05 18:59:24	14005	Hora
68516352	2019-01-05 21:01:06	14005	Hora
68515584	2019-01-05 22:16:52	14005	Hora
68515328	2019-01-06 08:18:10	14005	Hora
68516864	2019-01-06 10:25:56	14005	Hora

^aThe programs listed here are Fazio & Megeath (2004b, Program 6), Fazio & Megeath (2004c, Program 202), Kirkpatrick et al. (2010, Program 70062), Kirkpatrick et al. (2011, Program 80109), Getman et al. (2012), and Hora et al. (2018, Program 14005).

for each AOR to correct for any remaining background structure. We also used the artifact correction software *imclean* v3.2 (Hora 2021) to correct the remaining column pull-down and banding effects that occur for bright stars. We used the IRACproc mosaicking software (Schuster et al. 2006) to combine the data into one “long frame” (using the 12 and 30 second images) and one “short frame” (using the 0.6 and 1.2 second images) mosaic for each band. A color image of the final long frame 3.6 μm mosaic (and the *WISE* 12 and 22 μm images) is shown in Figure 1.

2.2. *MIPS*

Several areas of special interest were imaged previously by *Spitzer*’s Multi-Band Imaging Photometer (MIPS; Rieke et al. 2004) at 24 μm in Programs 6 and 202 (see Table 1). We obtained the post-BCD level 2 mosaics from the *Spitzer* Science Center.

2.3. *WISE*

The *Wide-field Infrared Survey Explorer* (*WISE*; Wright et al. 2010) mission surveyed the entire sky in

four infrared bands: 3.4, 4.6, 12, and 22 μm . While the *WISE* images allowed us to detect IR emission and identify molecular clouds and massive stars, *WISE*'s resolution ($\sim 6''$ at 3.4 μm) limits its ability to resolve the low-mass young stars in this region, which are typically found in spatially dense clusters and can result in source confusion. We therefore relied primarily on our IRAC catalog (with a point spread function FWHM of $1''.8$), cross matching our detected sources with *WISE* to include photometry in the 12 and 22 μm bands. In addition to providing higher confidence in the reliability of the cross matched sources, the supplemental photometry helped us construct the SEDs that we used to classify YSOs (see Section 6).

We obtained the *WISE* photometry from the All-*WISE* Source Catalog in the NASA/IPAC Infrared Science Archive. We queried a region with $355^\circ < \alpha < 7^\circ$ and $66.3^\circ < \delta < 70^\circ$. Because of the irregular edges of the IRAC mosaic, we chose a region that is considerably larger than the area covered by the IRAC images. Therefore, while this query resulted in a data set of 339,806 sources, only 144,280 sources were within $10''$ of an IRAC source (in the vicinity of the area covered by our IRAC mosaics).

2.4. 2MASS

The Two Micron All Sky Survey (2MASS; [Skrutskie et al. 2006](#)) survey imaged nearly the entire sky in the near infrared *J*- (1.25 μm), *H*- (1.65 μm), and *K_s*- (2.16 μm) bands. As with *WISE*, we cross matched our IRAC sources with the publicly available 2MASS photometric catalog from the NASA/IPAC Infrared Science Archive. We queried the same region described in Section 2.3 from the 2MASS All-Sky Point Source Catalog. We obtained a 2MASS data set of 310,956 sources, with 144,065 within the region covered by the IRAC mosaics.

2.5. MMIRS Near-IR Imaging

Near-IR images were obtained at *J*, *H*, and *K* with the MMT and Magellan Infrared Spectrograph (MMIRS; [McLeod et al. 2012](#)) at the MMT on Mt. Hopkins, AZ on several nights in 2019 December - 2020 January (program SAO-8-19c) and 2020 December - 2021 January (program SAO-12-21a). The instrument field of view (FOV) is $\sim 6.9' \times 6.9'$ in size, with $0''.2$ pixels. The typical seeing-limited point source FWHM sizes were in the range $0''.5 - 0''.7$. A large area was mapped by performing several dithered frames at each position and then offsetting by the FOV size to a new position for another set of dithered frames. The data were first processed using the MMIRS pipeline ([Chilingarian et al. 2015](#)) to perform the sample-up-the-ramp and linearization corrections. The images were then background-subtracted

and mosaicked by a custom reduction program which uses tools in the *astropy* package ([Astropy Collaboration et al. 2013, 2018](#)) to align and average the frames with outlier-rejection. The combined spatial coverage in each band is shown in Figure 2.

2.6. PanSTARRS Photometry

We used optical photometry from the PanSTARRS data release 2 ([Flewelling et al. 2020](#)) available on the Mikulski Archive for Space Telescopes¹. The PanSTARRS archive was searched for objects within $1''$ of the positions of the YSOs identified in Section 4. A total of 33 objects were found to match the positions of the YSO candidates identified from the IRAC data. The *r* and *i* band optical photometry of these sources was used in the SED fitting described in Section 6.

3. DATA REDUCTION

3.1. IRAC Photometry

We performed photometry on the IRAC mosaics using *Source Extractor* (SExtractor; [Bertin & Arnouts 1996](#)). The details of the source extraction and photometry are provided in Appendix A.1. We then matched sources in the short and long frame catalogs for each IRAC band. We used the difference in long and short frame magnitude to determine an appropriate magnitude cutoff to account for saturation in the long frame exposures. We obtained magnitude cutoffs of 10.8, 10.3, 9.5, and 9.2 for bands 1, 2, 3, and 4 respectively by identifying the brightest magnitude above which there was significant disagreement between the short and long frame magnitudes. For sources brighter than the cutoff, we replaced the magnitudes from the long frame mosaics with the values obtained from the short frame mosaic. In the case that one source had a magnitude below the cutoff and the other above (for example if the long frame magnitude was brighter than the cutoff and the short frame magnitude fainter than the cutoff), we used the short frame value. There were several bright sources in each band that were detected in only one of the two exposures (18 in band 1 and 73 in band 2, 7 in band 3, and 13 in band 4). These sources were examined manually and found to be either false detections or true detections whose positions were affected by saturation. These sources were included or excluded from the catalogs appropriately.

We performed the source extraction again using a separate set of extraction parameters for the long frame images in the Be 59 region. This region is significantly

¹ <https://archive.stsci.edu/panstarrs/>

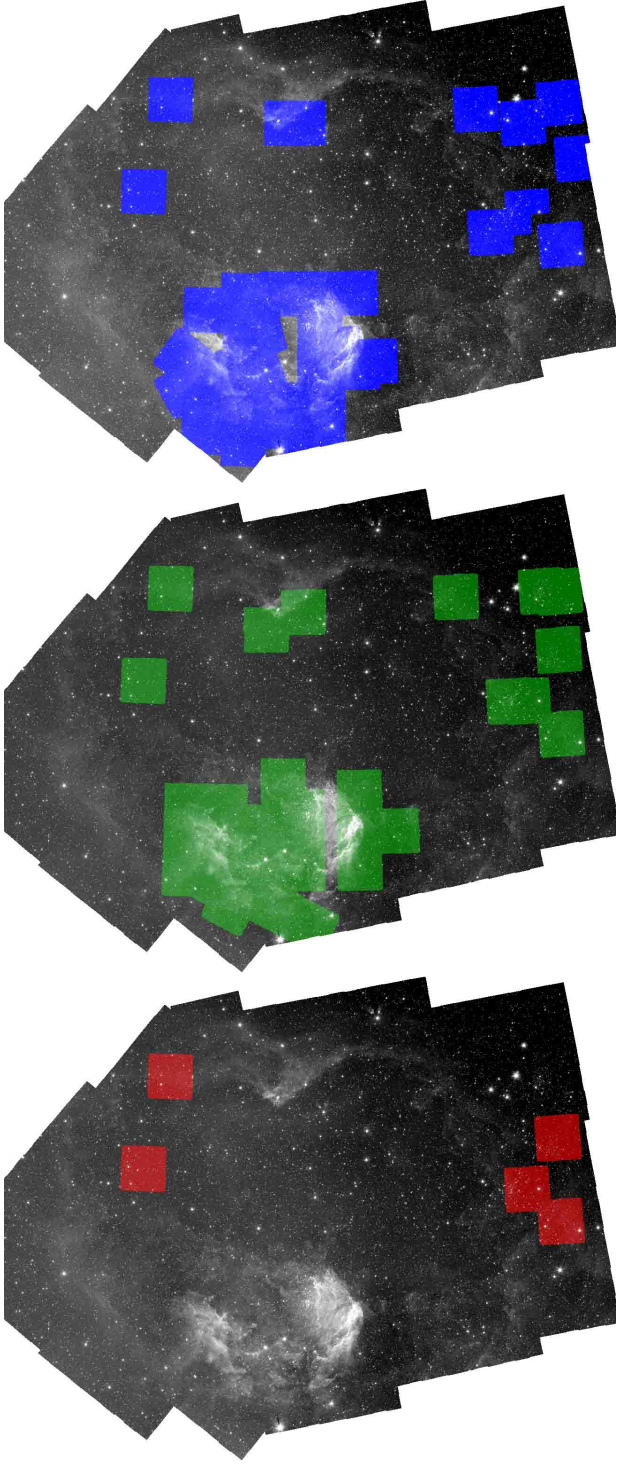


Figure 2. The near-IR MMIRS coverage, plotted on the IRAC 4.5 μm image of Cep OB4. Top: the MMIRS *J*-band sources plotted in blue. Middle: the MMIRS *H*-band sources plotted in green. Bottom: the MMIRS *K*-band sources plotted in red.

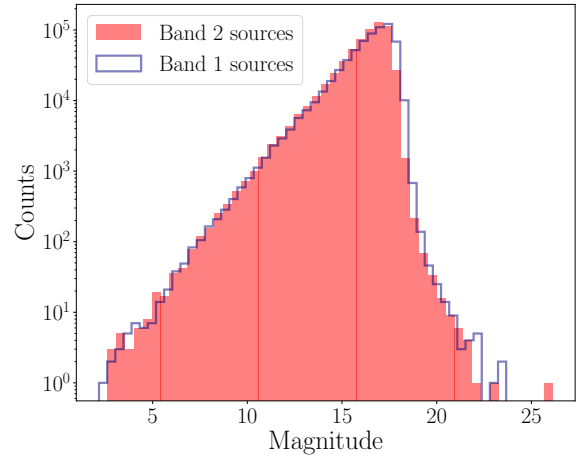


Figure 3. Histograms of detected source magnitudes for IRAC bands 1 and 2, with counts plotted on a log scale. Band 1 sources are plotted in navy and band 2 sources are plotted in red. The number of sources peaks at about 17 magnitudes and drops sharply dimmer of 17 magnitudes. This drop reflects the lower limit of our detection capability.

more nebulous than the rest of the field and so extracting an optimal number of sources required different background parameters. We only included sources from this Be 59 extraction that were not present in the previous extractions, adding an additional 18,818 source in band 1 and 16,296 in band 2.

After replacing saturated long frame values with the short frame photometry and adding the additional Be 59 sources, we obtained a band 1 catalog of 654,850 sources and a band 2 catalog of 616,570 sources. Histograms of the band 1 and band 2 magnitudes of detected sources are shown in Figure 3. We then matched the band 1 and band 2 sources obtained from our data using a cross matching distance of $1''.5$ to create a single catalog of sources with magnitudes in at least one band. Our final catalog derived from our IRAC band 1 and 2 data contained 752,615 total unique sources; 69% had measured magnitudes in both bands, 18% had magnitudes only in band 1, and 13% had magnitudes only in band 2.

After compiling the IRAC catalog in bands 1 and 2, we cross matched with the catalogs from bands 3 and 4. We only included band 3 and 4 sources that had corresponding sources in bands 1 or 2. We found 714 cross matched sources with photometry in bands 3 and 4, 1,437 with photometry only in band 3, 927 sources with photometry in only band 4, and 749,537 sources with photometry in neither band 3 nor band 4. The small number of band 3 and 4 sources is due only to the limited coverage of the band 3 and 4 images.

3.2. MIPS 24 μm Photometry

We performed photometry on the MIPS 24 μm images using SExtractor, finding 1882 sources. Parameters and details of the process are given in Appendix A.1.

3.3. MMIRS Photometry

We performed photometry on the MMIRS images using SExtractor with parameters optimized for the spatial resolution and background characteristics of the MMIRS images. The details of the process are given in Appendix A.2. After calibration, all sources in each band were merged into one catalog using a cross matching distance of $2''$. We obtained catalogs with 158,526 J-band sources, 177,510 H-band sources, and 7,613 K-band sources.

3.4. Cross Matching

Using our complete IRAC catalog obtained via the methods described in Section 3.1, we cross matched our IRAC sources with the *WISE* and 2MASS databases described in Sections 2.3 and 2.4. We used a cross matching distance of $1''.5$ and found 13% of our sources had corresponding *WISE* and 2MASS photometry, 6% of our sources had 2MASS but no *WISE* photometry, 4% of our sources had *WISE* but no 2MASS photometry, and 77% had neither *WISE* nor 2MASS photometry. While we did not investigate the false matching rate rigorously, we do not expect it to be significant considering that the mean positional error for IRAC sources with respect to 2MASS sources is $0''.25$ (Fazio et al. 2004a).

We also cross matched our catalog with the extracted catalog of MIPS 24 μm photometry described in Section 3.1 using a radius of $2''$. We found 485 MIPS sources with corresponding IRAC photometry. This small number of matched sources is again due to the limited coverage of the MIPS images.

Lastly, we cross matched the MMIRS near-IR photometry with the compiled catalog. Matching MMIRS required additional consideration to account for the difference in MMIRS and IRAC resolution. We used a matching distance of $1''.5$ and flagged any IRAC sources with multiple close MMIRS source – a potential indication of unresolved stars in the IRAC images. If one of the close MMIRS sources was at least one magnitude brighter than the other neighbors, we assumed the IRAC photometry was not detrimentally affected by the unresolved neighbors and we flagged the source as a good multi-match. If all of the MMIRS close neighbors were of comparable brightness, then the IRAC photometry likely did not accurately correspond to the MMIRS photometry and we flagged such sources as bad multi-matches and did not include them in the MMIRS YSO

selection in Section 4.4. Of the 146,344 MMIRS source that matched to an IRAC source 4% had good multi-matching and 5% had bad multi-matching.

4. YSO IDENTIFICATION AND CLASSIFICATION

We identified the YSO candidates in our compiled catalog by selecting objects with excess IR emission, a result of the reprocessed stellar radiation from the cool, dusty material in the surrounding circumstellar disks and envelopes. After removing background sources, we selected the YSO candidates using various color-color cuts to distinguish them from cool or reddened stars (Allen et al. 2004; Gutermuth et al. 2004; Winston et al. 2007, 2020). Hereafter we will refer to the YSO candidates as “YSOs,” but a definitive classification would require a more detailed analysis of the spectra and other characteristics of each object.

In this section, we present the criteria used in the YSO selections for each subset of our catalog. After identifying the YSOs, we classify their evolutionary stages based on the slopes of their SEDs between 2 and 20 μm .

4.1. 2MASS+IRAC

4.1.1. Background Sources

We anticipated that some of the detected sources with excess IR emission would be active galactic nuclei (AGN) or star forming galaxies (SFG) with polycyclic aromatic hydrocarbon (PAH) emission. Foreground PAH emission is also a potential source of aperture contamination that could affect a source’s measured photometry. The region will also have many main sequence stars in the foreground and background that are unrelated to the Cep OB4 clusters. We refer to all such sources as background sources (acknowledging that some stars and PAH emission may actually be foreground contamination) and removed them before proceeding with the YSO selection. We follow the selection criteria described in Winston et al. (2020), which is adapted from Winston et al. (2019); Gutermuth et al. (2008, 2009) and reported in Appendix B.

The result of the background source identification is shown in Figure 4. Of the 752,615 sources, we classified 711,152 (94.5%) as background sources and 41,463 (5.5%) as potential YSOs to be evaluated further. In the following sections, the 2MASS+IRAC YSO selections were based only on these 41,463 potential YSOs.

4.1.2. 2MASS+IRAC YSO Selection

We selected YSOs based on excess IR emission using 2MASS+IRAC bands in a variety of color-color combinations. Of the 41,463 sources evaluated, 99% had 2MASS photometry. We calculated the extinction coef-

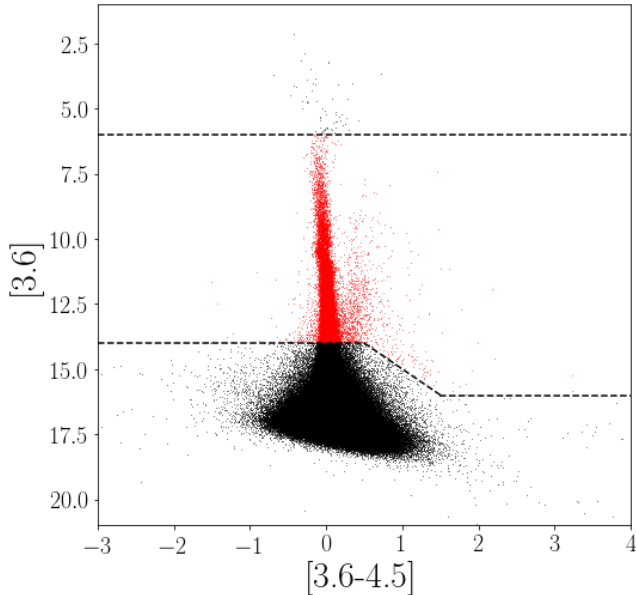


Figure 4. The results of the IRAC [3.6] versus [3.6-4.5] identification of background sources. The dashed black lines represent the selection criteria presented in Section 4.1.1 and Appendix B. The background sources eliminated from the YSO selection are shown in grey and the sources considered in the YSO evaluation are shown in red.

ficient A_{K_s} for each of these sources following the IR extinction laws described in Flaherty et al. (2007). We removed the 29 sources with non-valid values of extinction from our YSO selection, leaving 41,030 non-contaminant sources with good extinction values and 2MASS photometry.

We adapted the selection criteria from Winston et al. (2020). We aimed to include the maximal number of YSOs and so made the cutoff less conservative to encompass more sources. However, we wanted to minimize the number of non-YSO field stars selected, and so we examined the spatial distribution of the selected sources to confirm that the additional sources were not scattered randomly about the field, but instead were concentrated in clusters or located near pillars. This spatial distribution provided an additional confirmation of the validity of our selection. The criteria are reported in Appendix B and the results are shown in Figure 5. Of the 41,030 candidates, 719 were selected as YSOs, about 1.7%.

4.2. WISE

4.2.1. Background Sources

We followed the WISE contaminant removal procedure described in Winston et al. (2020) based on Fischer et al. (2016) and Koenig & Leisawitz (2014) to identify AGN and SFG in the subset of our catalog with

WISE photometry. The specific criteria for selection are described in Appendix C. Of the 126,835 sources with WISE photometry, 116,796 were identified as AGN and 68,634 were identified as SFG. This left 6,526 remaining WISE YSO candidates.

4.2.2. WISE YSO Selection

We identified YSOs from the remaining WISE YSO candidates using the four WISE photometric bands. The selection cuts are reported in Appendix C and shown in Figure 6. Of the 6,526 candidates, we identified 235 WISE YSOs, about 3.6%.

4.3. WISE & IRAC

We repeated the procedure for AGN and SFG removal and YSO selection described in Section 4.2 using the IRAC photometry for 3.6 and 4.5 μm instead of the WISE bands 1 & 2. This additional selection uses the shorter wavelength IRAC magnitudes, which may not have been reliably detected with WISE. We also excluded objects identified as background sources using IRAC and 2MASS in Section 4.1 from the YSO selection in this section.

Using these photometry, we found that of the 126,835 sources with WISE photometry, 111,879 were identified as AGN and 59,491 were identified as SFG. An additional 5,625 that were not identified as AGN or SFG were identified as background sources in Section 4.1 and were removed. This left 5,217 YSO candidates. Applying the same selection criteria as in Section 4.3, we identified 196 YSOs, about 3.7%.

4.4. MMIRS & IRAC

We repeated the background source removal and YSO selection described in Section 4.1, using MMIRS photometry in place of 2MASS. We only included sources with MMIRS photometry below the saturation limit: 12.7 magnitudes for H-band, 12.5 magnitudes for J-band, and 11.1 magnitudes for K-band. We also excluded sources that had corresponding 2MASS photometry above these limits as such sources were saturated and thus had unreliable photometry in the MMIRS images. These restrictions left 6,803 non-background sources with MMIRS photometry in the H-band, 8,501 J-band sources, and 1,408 sources in K-band. Of the 10,230 sources with good MMIRS photometry in at least one band, 232 were selected as YSOs, about 2.3%.

4.4.1. Comparing MMIRS and 2MASS YSOs

The MMIRS YSO selection yielded 53 additional YSOs that were not identified using 2MASS+IRAC in Section 4.1, an expected result as the MMIRS photometry is generally more reliable due to its higher resolution.

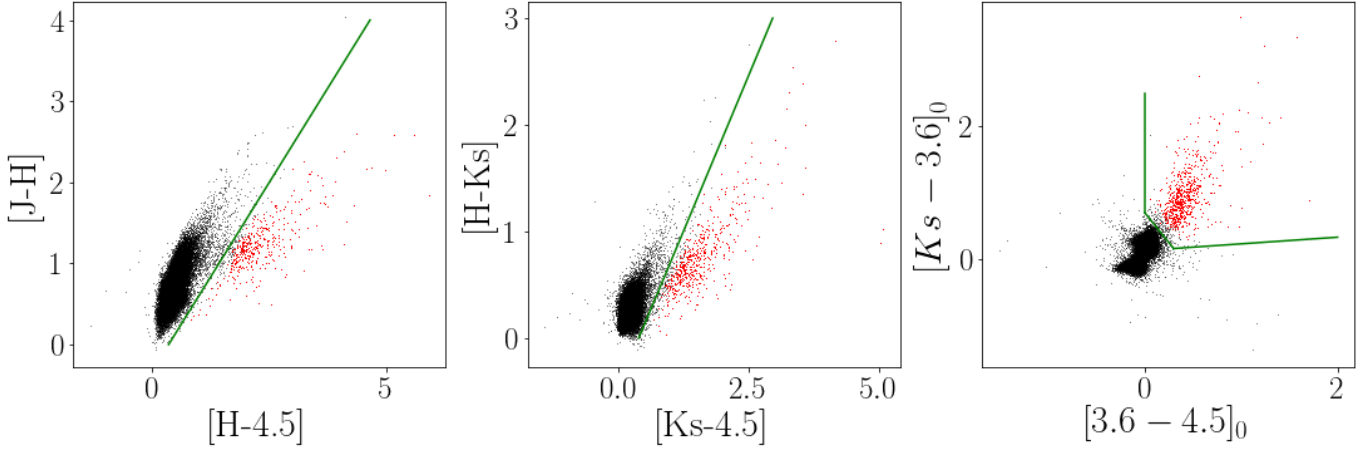


Figure 5. The results of the 2MASS+IRAC YSO selection. The green lines show the selection criteria described in Appendix B. The field sources not identified as YSOs are plotted in grey and the identified YSOs are plotted in red. The YSOs are identified by their excess IR emission. We identified 388 YSOs in the leftmost selection, 514 YSOs in the middle selection, and 656 YSOs in the rightmost selection.

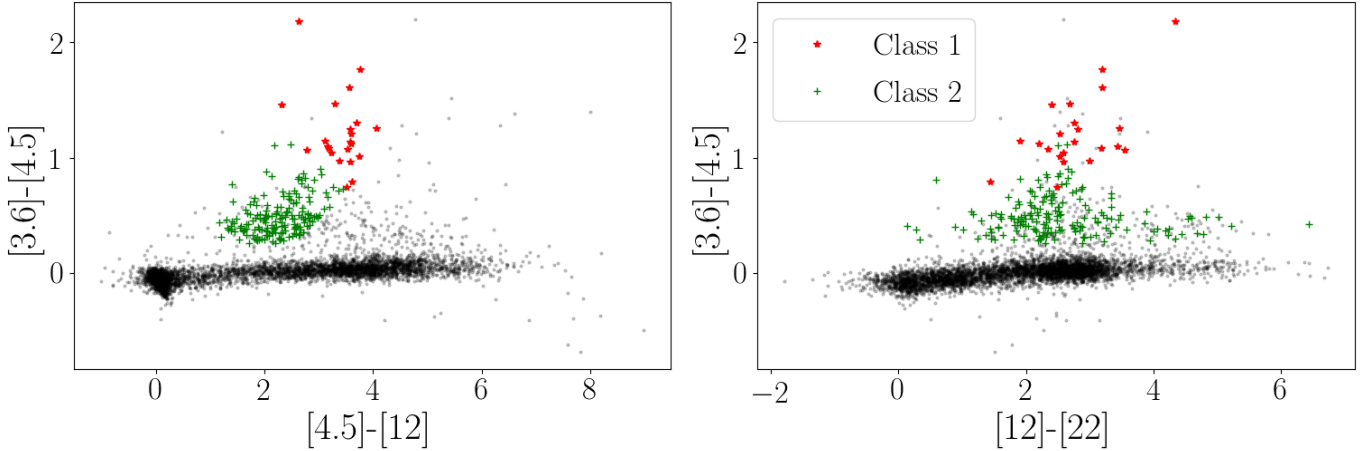


Figure 6. The results of the *WISE* & IRAC YSO selection described in Appendix D and Section 4.3. The red points are YSOs identified as Class 1, the green points are identified as Class 2, and the black points are the non-AGN non-SFG non-YSO sources. We identified 22 Class 1 sources and 174 Class 2 sources.

There were 28 YSOs identified using 2MASS+IRAC that had good MMIRS photometry in all of the necessary bands but were not selected as YSOs in the MMIRS cuts. As this represented a relatively small portion of the YSOs and there was no discernible trend in MMIRS and 2MASS magnitude differences in these sources, we attributed this difference to potential photometric uncertainties and intrinsic variability in the stars. We flagged these YSOs in our catalog, but retained them for subsequent analysis.

Another useful aspect of the MMIRS photometry is that it can reveal the presence of unresolved 2MASS sources that were selected as YSOs. Of the 221 2MASS YSOs with good corresponding MMIRS photometry in at least one band used for 2MASS selection that were

not selected as MMIRS YSOs, 6 were flagged as MMIRS sources with good multi-matching and 11 (with one overlap) were flagged as MMIRS sources with bad multi-matching as defined in Section 3.4. This represents a total of 16 2MASS YSOs that are potentially multiple unresolved stars. We flagged the sources as such, but retain them in our YSO catalog for subsequent steps of the analysis.

4.5. IRAC 5.8 & 8.0 μ m

In the regions with coverage in IRAC bands 3 and 4, we selected YSOs following the methods of Winston et al. (2019). The selection criteria are described in Appendix F. We identified 60 total YSOs, 9 of which were not identified using the selections in previous sections.

Table 2. Photometry Table Description

Column Number	Column ID	Description
0	Name	Source Name
1	RAdeg	Right ascension 2000 (degrees)
2	DEdeg	Declination 2000 (degrees)
3	MAGI1	IRAC 3.6 μm magnitude
4	e_MAGI1	IRAC 3.6 μm uncertainty
5	MAGI2	IRAC 4.5 μm magnitude
6	e_MAGI2	IRAC 4.5 μm uncertainty
7	MAGI3	IRAC 5.8 μm magnitude
8	e_MAGI3	IRAC 5.8 μm uncertainty
9	MAGI4	IRAC 8.0 μm magnitude
10	e_MAGI4	IRAC 8.0 μm uncertainty
11	jm2MASS	2MASS J-band magnitude
12	e_jm2MASS	2MASS J-band uncertainty
13	hm2MASS	2MASS H-band magnitude
14	e_hm2MASS	2MASS H-band uncertainty
15	km2MASS	2MASS K-band magnitude
16	e_km2MASS	2MASS K-band uncertainty
17	f_jm2MASS	2MASS J-band flag
18	f_hm2MASS	2MASS H-band flag
19	f_km2MASS	2MASS K-band flag
20	w1mpro	WISE band 1 magnitude
21	e_w1mpro	WISE band 1 uncertainty
22	w2mpro	WISE band 2 magnitude
23	e_w2mpro	WISE band 2 uncertainty
24	w3mpro	WISE band 3 magnitude
25	e_w3mpro	WISE band 3 uncertainty
26	w4mpro	WISE band 4 magnitude
27	e_w4mpro	WISE band 4 uncertainty
28	f_w1mpro	WISE band 1 flag
29	f_w2mpro	WISE band 2 flag
30	f_w3mpro	WISE band 3 flag
31	f_w4mpro	WISE band 4 flag
32	MAGMIPS	MIPS 24 μm magnitude
33	e_MAGMIPS	MIPS 24 μm uncertainty
34	MAGJMMIRS	MMIRS J-band magnitude
35	e_MAGJMMIRS	MMIRS J-band uncertainty
36	MAGHMMIRS	MMIRS H-band magnitude
37	e_MAGHMMIRS	MMIRS H-band uncertainty
38	MAGKMMIRS	MMIRS K-band magnitude
39	e_MAGKMMIRS	MMIRS K-band uncertainty
40	YSO	YSO flag

4.6. MIPS 24 μm

In the regions with MIPS 24 μm coverage, we selected YSOs following the methods of [Winston et al. \(2019\)](#). The selection criteria are described in Appendix G. We identified 39 total YSOs, 10 of which were not identified using IRAC bands 1 and 2, 2MASS, MMIRS, and *WISE* photometry.

4.7. Combined YSO Catalog

2MASS+IRAC

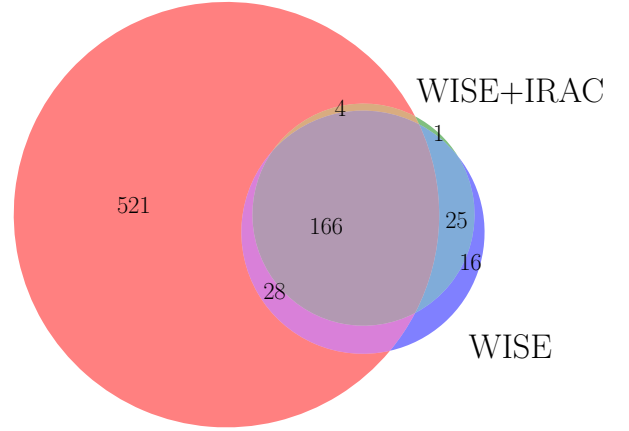


Figure 7. A Venn diagram showing the breakdown of YSO classification methods (excluding the selections based on IRAC bands 3 and 4 described in Section 4.5, MIPS 24 μm described in Section 4.6, and MMIRS described in Section 4.4, which are all restricted by limited spatial coverage). The vast majority of the YSOs were identified using 2MASS+IRAC photometry only.

After performing each of the selections described above, we merged all of the YSOs into a single catalog. Five YSOs were removed upon visual inspection as they appeared to have unreliable photometry resulting from poor extraction in especially nebulous regions. We describe the resulting photometric catalog in Table 2. Our final YSO catalog included 821 sources. 22.0% identified in all three selections, 68.1% identified in 2MASS+IRAC only, 2.1% in *WISE* only, 0.1% in WISE+IRAC only. A breakdown of the selection results are shown in Figure 7. Note that this figure does not include the results of the YSO selections using IRAC bands 3 and 4, MIPS 24 μm , or MMIRS. We excluded these sources from the summary chart as their selection statistics are representative only of the limited field coverage.

In following sections, when we reference our sample of YSOs, we refer to this merged catalog.

4.7.1. Evolutionary Classification

YSOs are typically classified into a number of evolutionary stages, ranging from embedded protostars to pre-main sequence YSOs ([McKee & Ostriker 2007](#)). We classified the YSOs in our sample following the classification scheme developed by [Andre et al. \(2000\)](#).

We calculated the slope of the SED over the wavelength range of 2-20 μm defined as $\alpha_{IR} \equiv \frac{d \log F_{\lambda}}{d \log \lambda}$ ([Lada 1987](#)). This included photometry in the K-band from 2MASS or MMIRS, in bands 3.6, 4.5, 5.4, and 8.0 μm from IRAC, and in bands 12 and 22 μm from *WISE*.

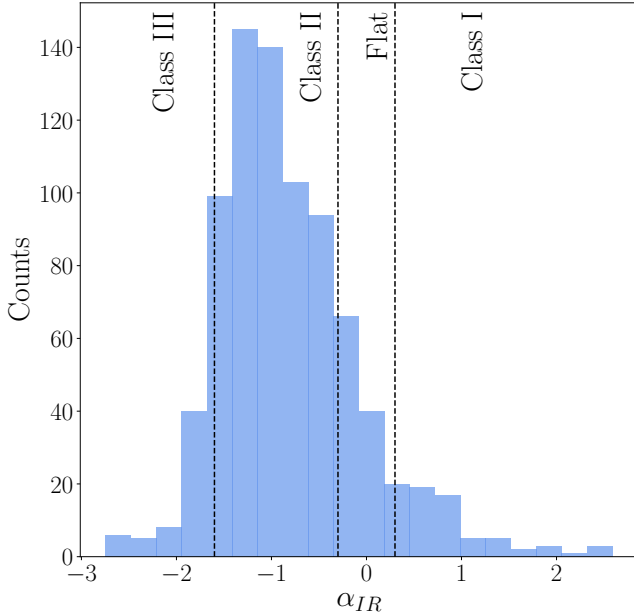


Figure 8. A histogram of the SED slopes α_{IR} of the YSOs. The black dashed lines at $\alpha_{IR} = -1.6, -0.3, 0.3$ show the cutoffs used in the evolutionary classification. Class 0 and I objects have $\alpha_{IR} \geq 0.3$, flat spectrum sources have $-0.3 < \alpha_{IR} < 0.3$, Class II sources have $-1.6 < \alpha_{IR} \leq -0.3$, and Class III have $\alpha_{IR} \leq -1.6$.

We fit a line to the log-scaled SEDs using the mean squared error minimization algorithm implemented in NumPy’s `polyfit`. To account for potential contamination in the lower resolution *WISE* photometry, we identified sources whose α_{IR} changed signs when including *WISE* 12 and 22 μm photometry. We fit α_{IR} on these 115 sources using only K-band and IRAC photometry. We used MMIRS photometry in place of 2MASS photometry for the K-band when available.

We used the α_{IR} cutoffs given in Andre et al. (2000) to classify the YSOs: Class 0 and I objects (protostellar) have a rising slope, $\alpha_{IR} \geq 0.3$, Class II sources have decreasing slopes between $-1.6 < \alpha_{IR} \leq -0.3$, and Class III have $\alpha_{IR} \leq -1.6$. We classify sources with $-0.3 < \alpha_{IR} < 0.3$ as flat spectrum sources.

We classified 67 of our YSOs as Class I, 103 as flat spectrum sources, 569 as Class II, and 82 as Class III. A histogram of these results is shown in Figure 8.

5. YSO DISTRIBUTION

5.1. Clustering

5.1.1. DBSCAN

We expected the identified YSOs to be clustered together (in the area of Be 59 for example) or in molecu-

lar pillars towards the edges of the H II region and not dispersed randomly over the field. To analyse this clustering, we used a method called “Density-based spatial clustering of applications with noise” (DBSCAN; Xu et al. 1997). This method identifies clusters by grouping points with many neighbors and flagging points with few neighbors as outliers. We used the DBSCAN implementation in Python’s SKLEARN package.

The DBSCAN algorithm requires two input parameters: ϵ and MnPts. The scaling size parameter, ϵ controls the bandwidth used to classify close neighbors. MnPts defines the smallest number of samples in a neighborhood required for a point to be considered as a core point. To determine the optimal values of these parameters, we followed the approach of Winston et al. (2019, 2020) based on the analysis of the Taurus region done by Joncour et al. (2018).

We chose ϵ as the turnoff value in the one-point correlation function (OPCF). The OPCF is calculated as the ratio of the cumulative distribution of nearest neighbors of the true distribution and a randomly generated distribution of the same number of sources spread over the same area. For a given separation ϵ , the cumulative distribution of nearest neighbors counts the number of sources with a neighbor within a radius of ϵ . When the OPCF is greater than 1, there are significantly more nearest neighbor pairings than there are in the randomly generated sample. When the OPCF is less than or equal to 1, the number of nearest neighbors in the true distribution is comparable to that of the random distribution. Therefore, we choose the value of $\epsilon = 0''.045$ at the turnoff point in the OPCF as seen in Figure 9 to minimize detections of random clustering.

The value of MnPts was determined by choosing the smallest number of points that results in a value of 0.001 for the cumulative distribution of nearest neighbors evaluated at $\epsilon = 0''.045$. This represents a probability of 0.001 of randomly finding a cluster of size MnPts for a scale factor of ϵ . We chose MnPts = 9 as shown in Figure 9.

While the spatial distribution of YSOs identified using MMIRS, MIPS, and IRAC bands 3 and 4 is biased by the limited coverage of these images, we did not find a significant difference in clustering results when they were included. This is likely due to the concentration of coverage in Be 59 and the northern region around IRAS00013+6817 where there are dense clusters of 2MASS and *WISE* YSOs. For this reason, we did not exclude these sources from our clustering analysis.

5.1.2. Cluster Properties

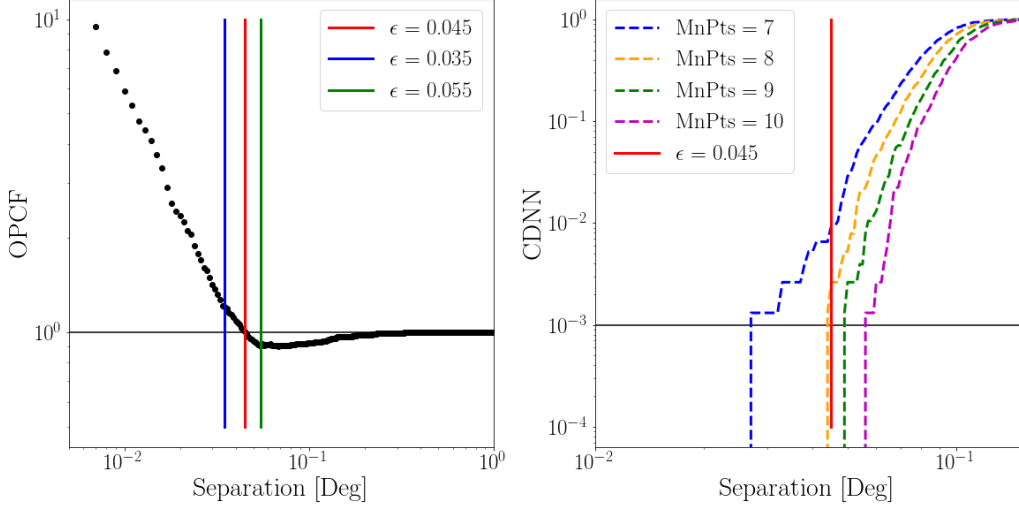


Figure 9. (Left) The one point correlation function used to determine the optimal value of ϵ , the bandwidth used for DBSCAN. The red line indicates the chosen value of $\epsilon = 0.045$ selected at the point with $\text{OPCF} \approx 1$. (Right) The cumulative distribution of nearest neighbors used to determine the optimal value of MnPts. When MnPts = 9, the probability of finding a random cluster for $\epsilon = 0.045$ is less than 0.1%.

Table 3. Cep OB4 YSOs

YSO ID	R.A. deg	Decl deg	YSO Selection Method ^a	Evo. Class	α_{IR}	$\sigma_{\alpha_{IR}}$	Cluster Membership
SSTCOB4 J23470610+6745164	356.7754205	67.7545648	000100	II	-0.91	0.37	—
SSTCOB4 J23473479+6751001	356.8949644	67.8500461	000100	Flat	-0.02	0.12	—
SSTCOB4 J00095102+6842133	2.4625862	68.7037036	000100	Flat	-0.13	0.30	—
SSTCOB4 J00102105+6845167	2.5877272	68.7546457	000100	III	-2.03	0.17	—
SSTCOB4 J00114782+6847195	2.9492560	68.7887726	100100	Flat	-0.25	0.05	—
SSTCOB4 J00115485+6806090	2.9785559	68.1025245	000100	I	0.66	0.14	—
SSTCOB4 J23474717+6748538	356.9465785	67.8149459	000100	II	-1.33	0.36	—
SSTCOB4 J23484602+6803394	357.1917535	68.0609588	000100	I	0.85	0.18	—
SSTCOB4 J23465418+6817350	356.7257701	68.2930714	000100	I	0.48	0.20	—
SSTCOB4 J23473180+6818507	356.8825085	68.3140956	100000	III	-2.25	0.47	—

(This table is available in its entirety in machine-readable form.)

^aThe binary flag describes the selection method(s) used to identify the YSO with digits representing 2MASS, *WISE*, IRAC+*WISE*, MMIRS, IRAC bands 3 and 4, and MIPS selections respectively.

Using the parameters determined in Section 5.1.1 we identified 5 clusters of YSOs in Cep OB4, shown over the IRAC image in Figure 10 and shown individually in Figure 11. About 63% of the identified YSOs were assigned to clusters with the remaining 37% unclustered. The largest cluster size was 445 and the smallest was 6. The median cluster size was 11 and the mean was 103. The locations, sizes, and ratio of Class I and flat spectrum objects to Class II objects are reported in Table 4.

The rough area of each cluster was calculated by measuring the convex hull of the cluster members. The convex hull is the polygon formed by using cluster members as vertices so that all cluster members are included in

the polygon. The convex hulls of the clusters are plotted in Figure 10. The circular radius of a cluster is calculated as half the largest separation between two YSOs in the cluster.

The largest cluster is located in the center of Be 59, with two smaller cluster adjacent to it. A mid-sized cluster is located in the northern region in an area of dense nebosity near IRAS00013+6817. We note that the smallest cluster, Cluster #4 may be a chance over-density in the field and not a true stellar group. We did not assess the probability of random over-densities rigorously in this study.

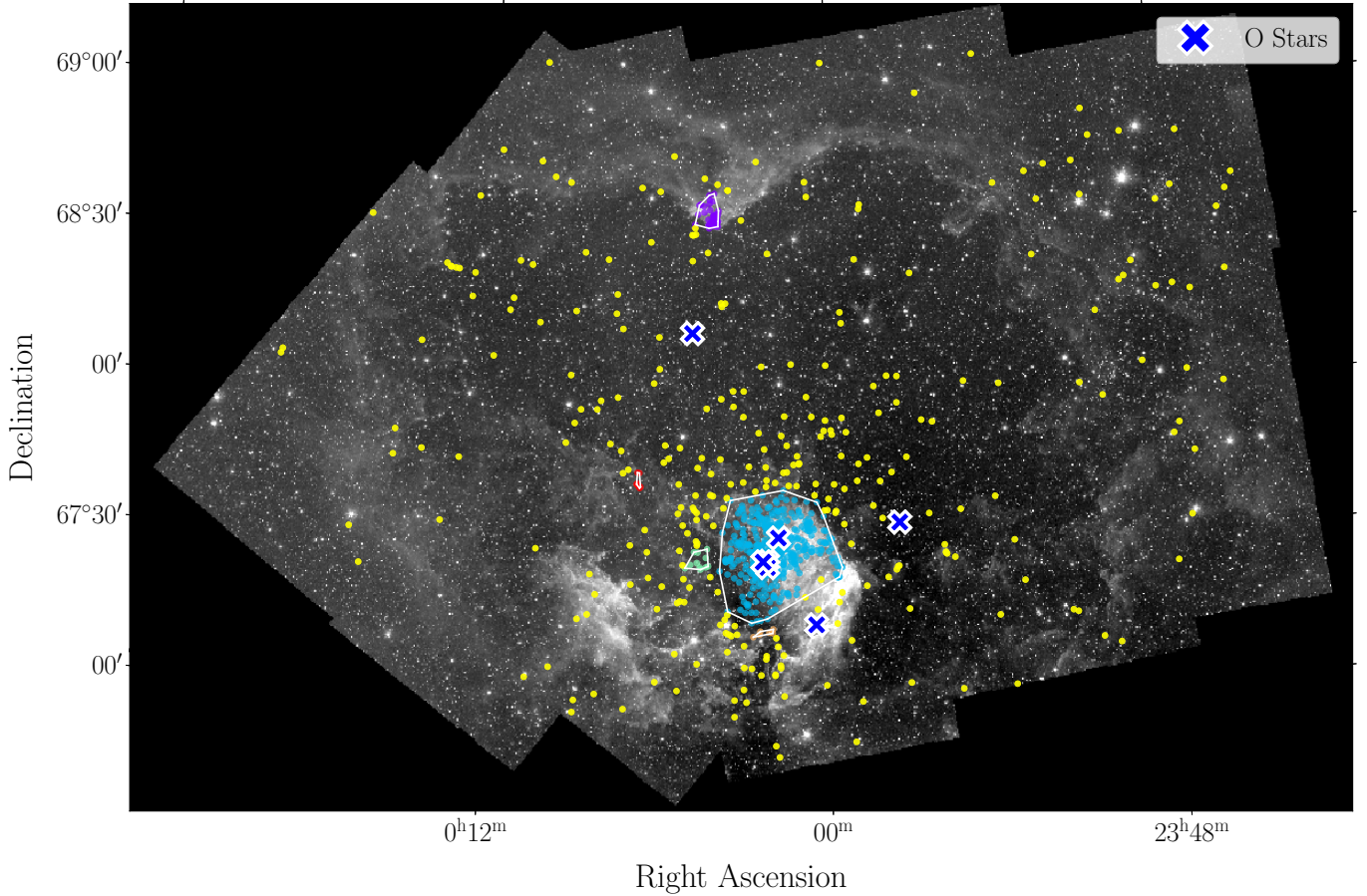


Figure 10. The identified YSOs and clusters shown over the IRAC 3.6 μm image. The five clusters are plotted in purple, blue, green, orange and red respectively. The YSOs that are not members of any cluster are shown in yellow. The convex hulls for each cluster are overlayed in white. The largest cluster (blue) is located in the Be 59 region. The characteristics of the clusters are reported in Table 4. The location of O-type stars cataloged in Skiff (2014) are plotted as blue x’s outlined in white.

We note that Cluster #1, the cluster encompassing the majority of Be 59 has the lowest ratio of Class I to Class II objects, indicating that its YSOs are older on average than the other clusters’ YSOs. The slightly higher ratio of the nearby clusters – Clusters #2 and #3 – suggests that these clusters are younger than the main central cluster and that star formation farther from the central O stars was triggered later. This conclusion is also supported by the higher ratio in the northernmost cluster. We elaborate further on the radial dependence of the Class I to Class II ratio in Section 5.2.

5.1.3. Subclustering in Be 59

To further analyze the YSO distribution in the Be 59 region, we reran the DBSCAN algorithm on the YSOs near Be 59. We selected only YSOs which were within

1.5 times the circular radius of Cluster #1 as reported in Table 4. Using the same method described in Section 5.1.1 we obtained DBSCAN parameters of $\epsilon = 0^{\circ}02$ and $\text{MnPts} = 9$. After running the algorithm with these parameters, we identified 5 subclusters in the Be 59 region. We report their properties in Table 5. We note that Subcluster #3 has a significantly higher ratio of Class I to Class II objects, indicating that it is younger than the rest of the subclusters and other sources in the central region. We attribute this difference in age to the location of Subcluster #3. It is situated in an especially dense, nebulous region. The material in the vicinity of Subcluster #3 was likely not evacuated by the shock-wave due to its density, leaving behind a concentration of molecular dust ready to be triggered. We suspect that the O stars which have remained near the center of Be 59 – including BD+66 1673, which is closest in projected distance to the subcluster – are responsible for catalyzing the collapse and the subsequent recent burst of star formation we see in Subcluster #3.

Table 4. YSO Cluster Properties

Cluster Number	Number of YSOs	Central RA (deg)	Central DEC (deg)	Circular Radius (deg)	Class I/Class II ^a	Color in Figure 10
0	46	1.033	68.578	0.060	0.375	purple
1	445	0.488	67.462	0.235	0.227	blue
2	11	1.135	67.428	0.049	0.375	green
3	6	0.568	67.190	0.036	0.500	orange
4	9	1.671	67.690	0.026	0.800	red

^aThis ratio is calculated as the number of Class I and flat spectrum objects (as defined in Section 4.7.1) over the number of Class II objects.**Table 5.** YSO Be 59 Subcluster Properties

Cluster Number	Number of YSOs	Central RA (deg)	Central DEC (deg)	Circular Radius (deg)	Class I/Class II ^a
0	214	0.533	67.459	0.119	0.137
1	14	0.759	67.487	0.026	0.182
2	20	0.316	67.438	0.029	0.250
3	20	0.184	67.545	0.028	4.000
4	9	0.879	67.432	0.016	0.000

^aThis ratio is calculated as the number of Class I and flat spectrum objects (as defined in Section 4.7.1) over the number of Class II objects.

5.2. Unclustered YSOs

As described in Section 1, it is believed that most YSOs form in dense clusters, often impacted by high-energy OB stars. We have identified a large number of YSOs in such clusters in Section 5.1. However, we also expected that many YSOs would not be associated with any groups. There are a number of reasons for the presence of unclustered YSOs. They could have been expelled from their birth cluster through interactions with other cluster members, drifted slowly away from a YSO group as the shockwaves expelled molecular material and changed the gravitational potential of the region, or they might have formed in their current location, never having been associated with a cluster. It is challenging to definitively distinguish between these scenarios without kinematic information on the sources. If we could measure the velocity of a source, we could determine whether it is travelling away from a cluster, perhaps indicating that it was once a member. In the absence of such data, we can only look at the unclustered distribution in aggregate, and make assumptions about the general trajectory of the YSOs.

As described in Section 5.1, we found 63% of our YSOs associated with clusters. This clustering fraction agrees with previous findings: Winston et al. (2019) found

62% of YSOs in clusters in the SMOG field, Winston et al. (2020) found 54% in the region mapped by the GLIMPSE360 program, Fischer et al. (2016) found 53% in the Cannis Major star-forming region, and Koenig et al. (2008) found between 40% and 70% in the W5 H II region depending on their clustering parameters.

We calculated the density of unclustered YSOs in binned annuli at various distances from the center of Cluster #1 as reported in Table 4. The resulting distribution is shown in Figure 12. The density of unclustered YSOs is highest in the bins that are closest to the central Be 59 cluster and decreases steeply with increasing projected distance. The density decreases by more than a factor of 2 from the first bin to the second bin - the difference in distance between the bin midpoints being nearly equal to the central cluster's radius. We also calculated the Class I/Class II (CI/CII) ratio in the annular bins as a function of distance from the center and show the results in Figure 12. The high density of sources at smaller distances and the similarity of the CI/CII ratios to those of the central clusters (a reasonable proxy for relative age) indicate that most of the unclustered YSOs near Be 59 were likely once cluster members themselves. While it is impossible to conclusively determine without velocity information, the age and density of the sources strongly support this conclusion.

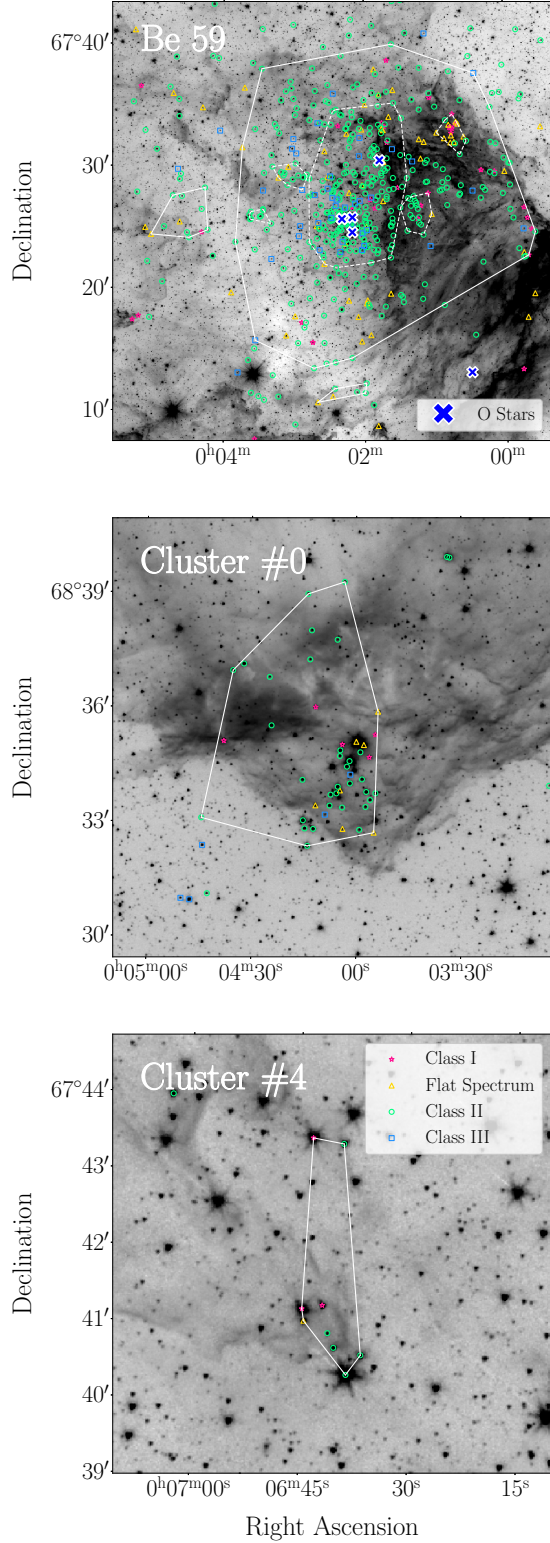


Figure 11. The five identified YSO clusters plotted over an inverted gray scale image at $3.6 \mu\text{m}$. The color and shapes of the YSOs indicate the evolutionary class as determined in Section 4.7.1. The white lines show the convex hulls of each cluster, with all cluster members included in the indicated region. The upper plot shows the Be 59 region with the convex hulls of the subclusters identified in Section 5.1.3 plotted in white dashed lines and the same O stars as in Figure 10.

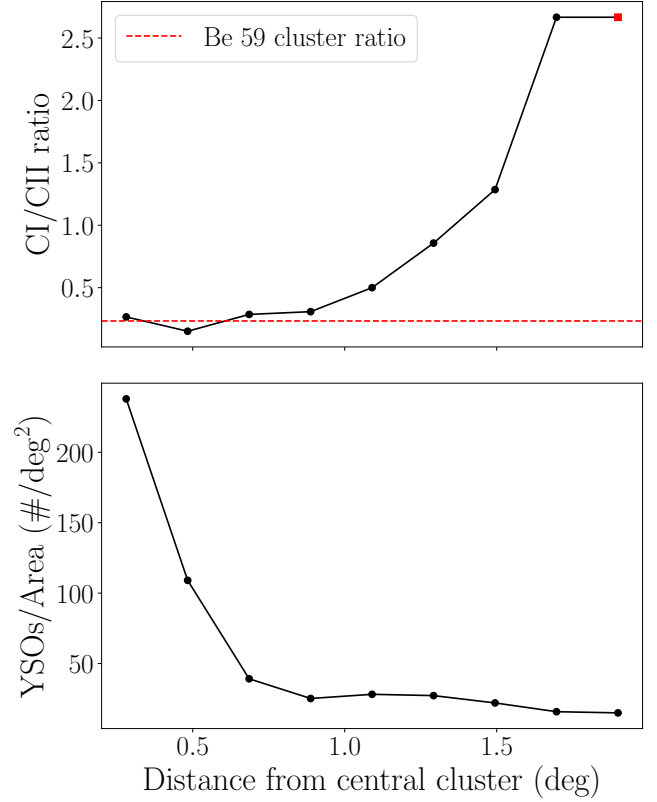


Figure 12. The distribution of unclustered YSOs. The top panel shows the Class I/Class II (CI/CII) ratio of YSOs in annular bins as a function of projected distance from the center of the Be 59 cluster found in Section 5.1. The red horizontal line indicates the CI/CII ratio of sources in the three central clusters. The value in the rightmost bin – marked by a red square – is undefined as there were no Class II sources in the final bin, and it is set to the same value as the previous bin. The bottom panel shows the density of the unclustered YSOs, normalized by the area in each annulus covered by the IRAC $3.6 \mu\text{m}$ mosaic. Both of these distributions provide evidence that many of the unclustered YSOs in the region’s center may have formed in the central clusters, and there is an age gradient with a higher fraction of younger YSOs at greater distances from Be 59, as described in Section 5.2.

The distribution of the CI/CII ratios is especially interesting in the context of triggered star formation. While the distribution of sources is much more complicated than a simple relationship between age and projected distance, the steeply increasing class ratio distribution indicates that (unclustered) YSOs in Cep OB4 are generally younger farther from the cluster’s center. This is evidence in favor of the collect and collapse model of triggered star formation, potentially demonstrating that the expanding shockwave did in fact trigger star formation as it travelled farther from its originating sources in the central cluster.

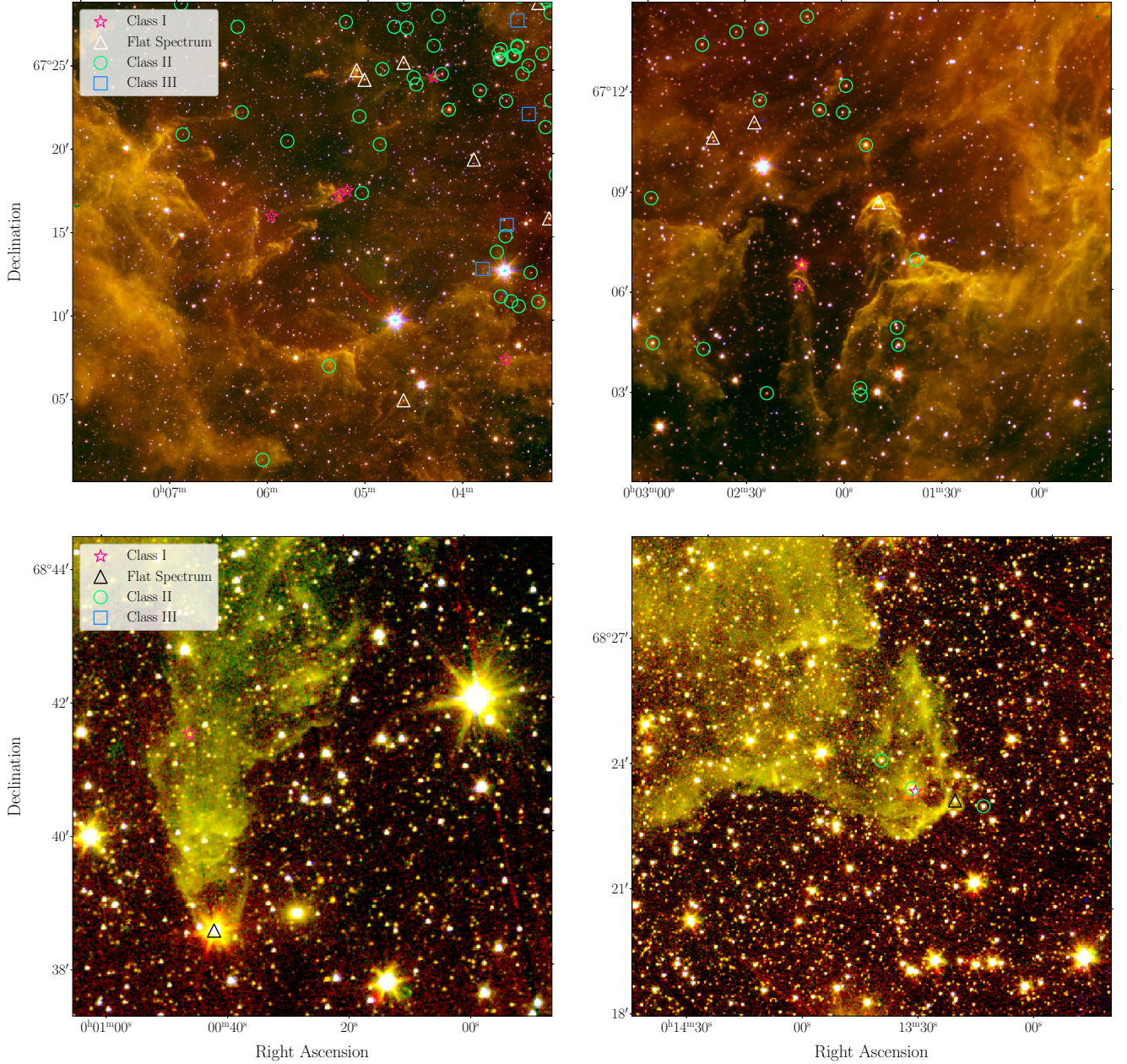


Figure 13. Four examples of identified YSOs located in molecular pillars. The YSOs are colored by evolutionary classification and plotted over a color image of 2MASS H-band $1.65 \mu\text{m}$ (blue), IRAC $3.6 \mu\text{m}$ (green), and IRAC $4.5 \mu\text{m}$ (red). The legends in the panels on the left also apply to the panels on the right in the same row. Pillars such as the ones visible in these images form when the ionizing winds from Be 59’s massive stars evacuate gas and dust around the cluster, leaving only the dense structures behind. Class I and flat spectrum sources are often seen at the tips of the pillars.

5.3. YSOs in Pillars

Another interesting aspect of the spatial distribution of our YSO sample is the presence of numerous YSOs in dense molecular pillars around the border of the H II region. We show several examples of YSOs in pillars in Figure 13 and YSOs in a dense molecular region in Figure 14. Such pillars are formed when the shock wave of the expanding H II region expels unbound dust and gas.

What remains around the edges of the bubble are the dense molecular filaments, often sites of star formation.

The presence of identified YSOs in these locations provides evidence in favor of triggered star formation, specifically for the radiation-driven implosion model described in Section 1. The expanding shockwave likely catalyzed collapse in pre-existing overdensities in Cep OB4, triggering star formation in exposed molecu-

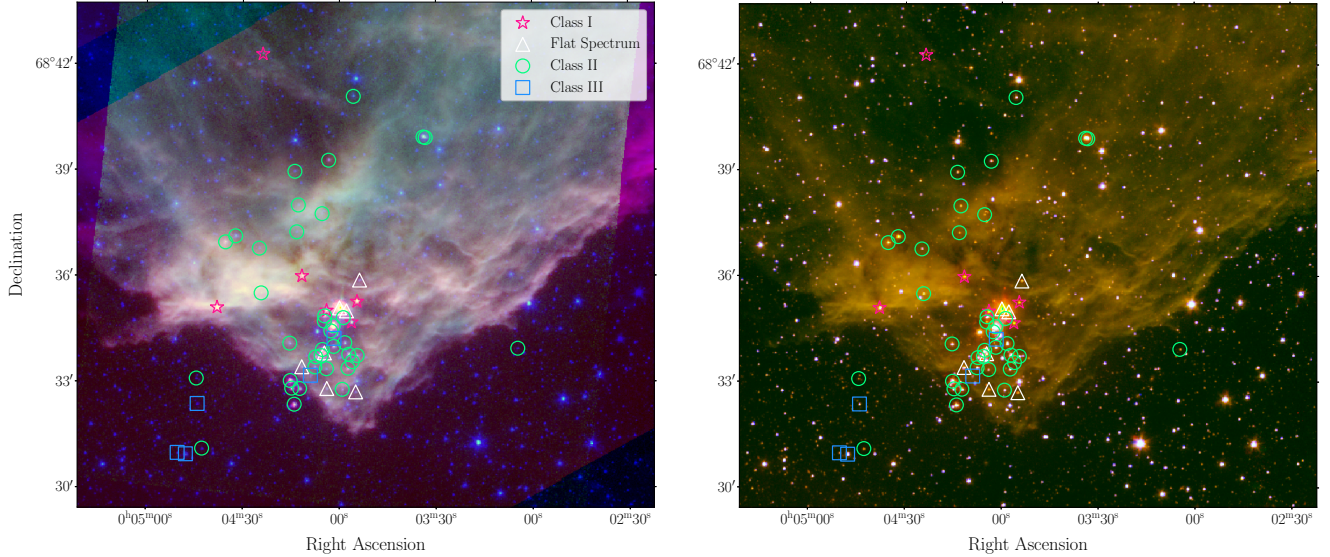


Figure 14. Identified YSOs in the northern region around IRAS00013+6817, colored as in Figure 13. (Left) A color image of IRAC 3.6 μm (blue), IRAC 8.0 μm (green) and MIPS 24 μm (red). (Right) Same as Figure 13 – a color image of 2MASS H-band 1.65 μm (blue), IRAC 3.6 μm (green), and IRAC 4.5 μm (red).

lar structures. In Figure 15, we show the approximate origins of the pillars as determined by their direction. It appears as though most of the pillars are pointing towards Be 59, specifically towards the four O stars in the central region: BD+66 1673, LS I +67 7, BD+66 1675, and NGC 7822 x. It is not possible for us to distinguish among these O stars due to the imprecision of our estimate of the pillar directions.

We also calculated the projected distance from the base and tip of the pillars to the center of the central cluster as reported in Table 4. We used an estimate for the shockwave expansion velocity of 15 km s^{-1} (e.g. Tiwari et al. 2021; Luisi et al. 2021; Patel et al. 1998) to estimate the age of the pillars and the shockwave. Including all of the pillars shown in Figure 15 resulted in an average expansion time of 1.2 Myr. However, it is important to consider the impact of projection effects. That is, the pillars in the south of the region appear very close to the central cluster even though they may be farther away in actual 3 dimensional space. If we only included the pillars farther to the north – those less affected by the limitations of projection – we calculated an average expansion time of 1.6 Myr. These rough estimates are consistent with Be 59’s age of 2 Myr as reported in Panwar et al. (2018). We also note that there is additional uncertainty in these estimates resulting from the imprecise definition of the “tip” or “base” of a pillar. However, the northern pillars had an average projected length of $\approx 3 \text{ pc}$, corresponding to an expansion time of $\approx 0.2 \text{ Myr}$, which would not significantly effect the age estimate of the OB association.

The length of the pillars and expansion velocity also provides an upper bound to the age of the YSOs forming in the pillars, assuming they started forming when the expanding shockwave first passed their location. The presence of primarily Class I and flat spectrum sources in the tips of the pillars (see Figures 13 and 14) are also consistent with this estimated age of the pillars.

6. SED MODEL FITTING

In Section 4.7.1 we used the YSO SEDs to separate the YSOs into evolutionary class. Here, we use the SEDFitter package in Python created by Robitaille et al. (2007) to more rigorously fit the YSO SEDs and obtain mass estimates. The SEDFitter package uses a sample grid of model SEDs with various ages and masses to fit the YSO distributions. If not specified, the object distance and extinction A_V are treated as free parameters. In our fitting, we allowed A_V to vary between 1 and 50, but set the distance to 1.1 kpc as determined in Kuhn et al. (2019).

We crossmatched our YSO catalog with sources from PanSTARRS as described in Section 2.6, finding 25 sources with photometry in bands r and i . We also matched our YSOs with the PMS sources published in Panwar et al. (2018), which is discussed further in Section 7.1 and found optical photometry in bands V and I for 109 of our YSOs.

We did not include the *WISE* 3.4 and 4.6 μm photometry in the SED fitting as we expect the IRAC 3.6 and 4.5 μm photometry to have more accurately separated sources in crowded regions, and including both would

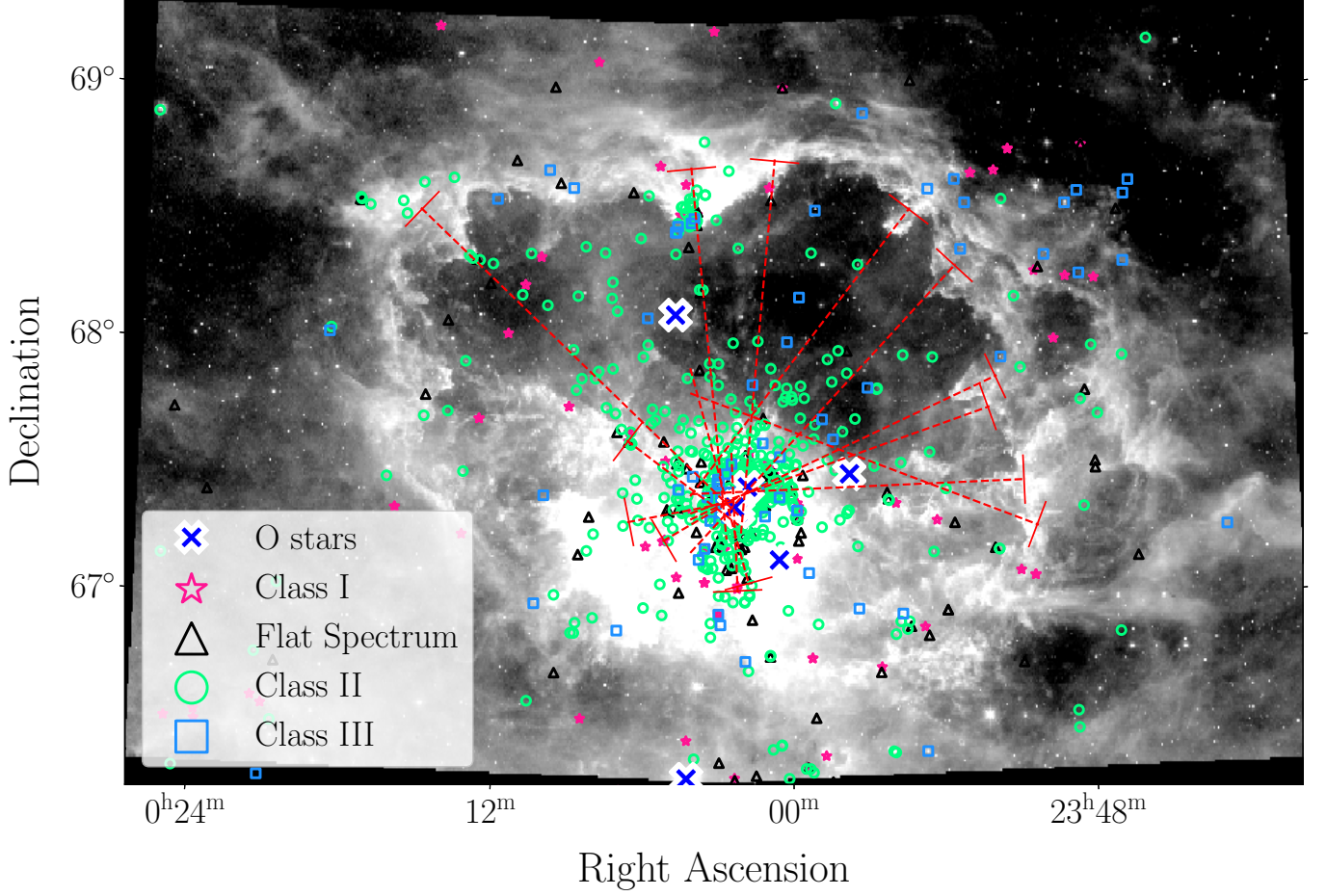


Figure 15. The location and direction of some of the pillars in Cep OB4 plotted over the *WISE* 12 μ m image. The dotted red lines begin at the base of the pillars (as indicated by the perpendicular line segment) and follow the pillar orientation to the center of region. The YSOs (including the *WISE*-only YSOs discussed in Section 7.2) are plotted with shapes and colors corresponding to their evolutionary classification as in Figure 13. The O stars in the region are plotted as blue x's outlined in white. It appears that most of the pillars were exposed by a shockwave originating from Be 59 – likely from one or all of the O stars in that region.

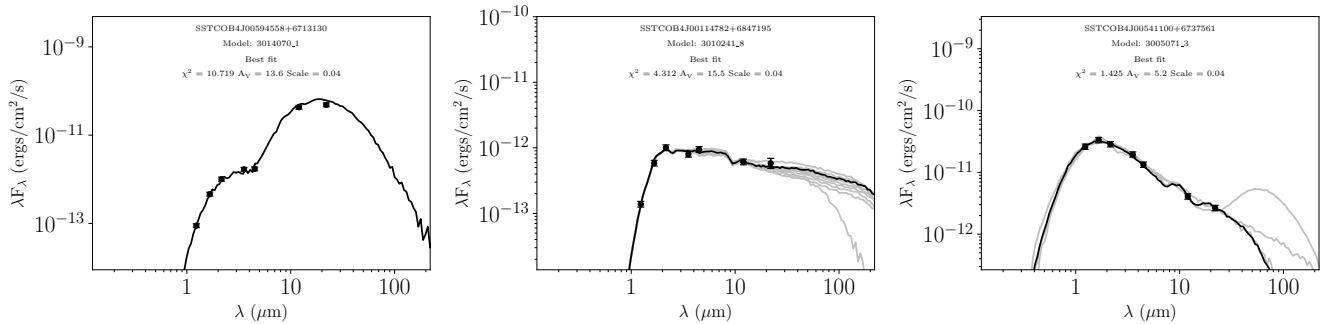


Figure 16. Three example fits of YSO SEDs (the complete set of plots of the YSO SED fits are available in the figure set). The leftmost SED is a Class I YSO, the center SED is a flat spectrum YSO, and the rightmost SED is a Class II YSO. The black points represent the photometric data and uncertainty. The black line indicates the best fit model SED and the grey lines show all model fits with $|\chi^2 - \chi^2_{best}| < 3$.

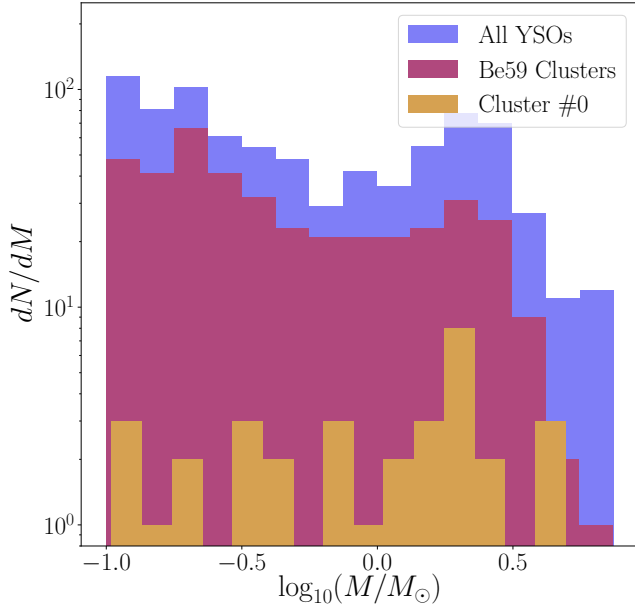


Figure 17. The initial mass functions as generated by the SED fitting for all of the YSOs, the YSOs in Cluster #0, and the YSOs in the clusters near Be 59. We only include SED results with $\chi^2 < 15$. The histograms are overlapping and not normalized. We see the same general trend in each of the samples, a trend that generally agrees with results from previous studies as discussed in Section 6.

result in unnecessarily inflated χ^2 for some fits. For sources without a *WISE* detection, we set upper limits at 12 and 22 μm of 10 and 8.5 magnitudes respectively, which are the approximate completeness limits of the *WISE* photometry in our sample. For sources with detections at MIPS 24 μm we used only the MIPS 24 μm data and excluded the *WISE* photometry as we considered MIPS to be more reliable because of its higher spatial resolution and better sensitivity. We also used MMIRS photometry when available in place of 2MASS values for the *JHK* bands. Lastly, we required all flux uncertainties to be at least 10% to take into account possible source variability and the true measurement uncertainties in the 2MASS, IRAC, MIPS, and *WISE* datasets. We report the results of the SED fitting in Table 6 and show some examples of good SED fits in Figure 16. (The complete set of plots of the SED fits is available in the figure set.)

Because most of our clusters contain a small number of YSOs, we are not able to compare the initial mass function across all clusters. However, we report the IMF for all YSOs, for Cluster #0, and for the clusters near Be 59 in Figure 17. We find that they are in general agreement with one another and with the IMF of all the YSOs together. While we did not have sufficiently many YSOs

to thoroughly compare these IMFs with those from previous studies, we note that the trends we find seem to be in agreement with those found in Winston et al. (2019) and Winston et al. (2020). While the results reported in Figure 17 use only YSOs with $\chi^2 < 15$ for their SED fit, we report all SED fits in Table 6.

7. RESULTS AND DISCUSSION

7.1. Comparison to Previous Studies

Getman et al. (2017) conducted a study of star formation in nearby clouds using X-ray and IR photometry. They employed a classification scheme slightly different than what we described in Section 4.7.1. They classified objects as “disk,” “no disk,” or “possible member of cluster”, with “disk” corresponding to what we describe as Class I, flat spectrum, and Class II, and “no disk” corresponding to Class III. There is good agreement between our catalogs for the “disk” sources – we were able to match 92% of the “disk” sources to our YSO catalog. The small differences in our catalogs can be attributed to slight differences in photometry and selection criteria. We do not compare the “no disk” or “possible member of cluster” sources as they were identified by Getman et al. (2017) using X-ray photometry.

We combined our YSO catalog with the additional Getman et al. sources and repeated the clustering analysis described in Sections 5.1 and 5.1.3. The addition of the extra sources did not significantly affect the YSO distribution or the clustering results. The one notable exception was the detection of an additional cluster in the northern region near our Cluster #0, where the additional sources added to an existing small group south-east of the cluster (see middle panel of Figure 11).

Panwar et al. (2018) also studied the Be 59 region, using optical photometry to identify pre-main-sequence stars. We matched the Panwar PMS sources with our YSO catalog using a matching radius of 1'' and found 109 of their 420 sources. There was a significant amount of disagreement between the masses reported in Panwar et al. (2018) and the masses that we derived via SED fitting without including optical photometry. When we included the optical photometry in the V and I bands and reran the SED fitting as described in Section 6, the agreement between masses increased significantly. More work is required to thoroughly identify the source of the discrepancy, but we note that the results of the SED fitting are sensitive to the inclusion of additional photometry. It is not immediately clear whether one set of mass values is more reliable than the other, and it

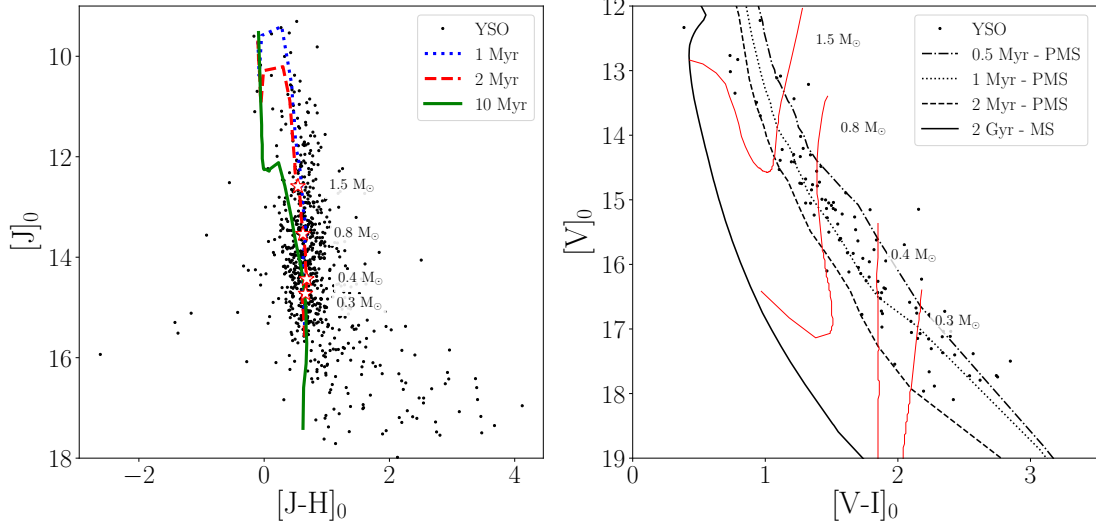


Figure 18. Near-infrared (left) and optical (right) color magnitude diagrams of our YSOs. PMS isochrones of various ages from [Siess et al. \(2000\)](#) are plotted in both figures. In the NIR CMD, we show the positions of stars of various masses on the 2 Myr PMS isochrone – shown as white stars outlined in red. In the optical CMD, we show the stars’ full evolutionary tracks – shown as solid red curves. A MS isochrone of 2 Gyr from [Girardi et al. \(2002\)](#) is shown in the optical CMD. The YSOs have been dereddened using the NICER extinction maps from [Lombardi & Alves \(2001\)](#). All of the isochrones and evolutionary tracks have been shifted using the assumed distance to Cep OB4 of 1.1 kpc.

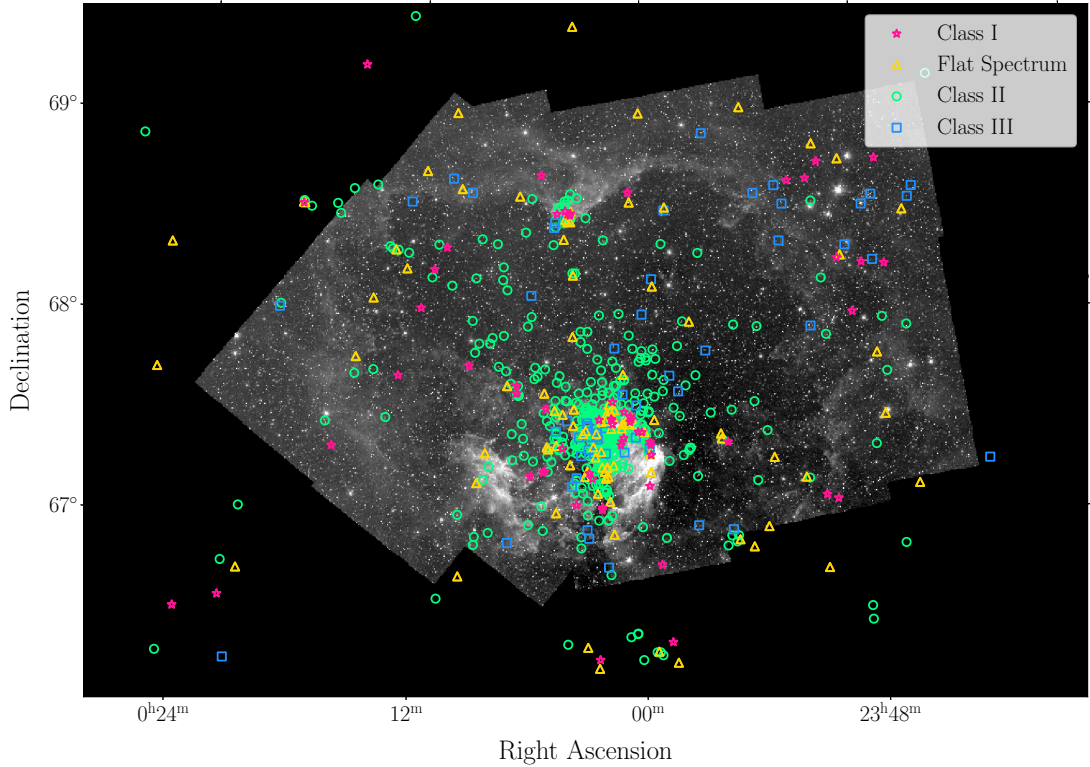


Figure 19. The spatial distribution of YSOs in Cep OB4 plotted over the IRAC 3.6 μ m image. Here we show the YSOs identified in Section 4 as well as those identified using the larger region queried from the *WISE* catalog as described in Section 7.2. The YSOs are colored by their spectral type. We see numerous young Class I and flat spectrum YSOs towards the outskirts of the cluster and fewer inside the dense border of the H II region, indicating that there may have been continuing star formation before the creation of the ionized bubble.

Table 6. SED Fitting Results

YSO ID	Dist (kpc)	N_{data}	χ^2	M_C (M_\odot)	A_V (mag)	Age (yr)	M_{disk} (M_\odot)	\dot{M} (M_\odot/yr)	T_* (K)	L_* (L_\odot)
SSTCOB4 J00470610+6745164	1.1	6	12.680	2.307	1.000e+00	1.676e+05	7.136e-02	2.178e-04	4.441e+03	3.409e+01
SSTCOB4 J00473479+6751001	1.1	7	17.790	0.978	1.153e+00	6.726e+05	5.654e-04	6.875e-09	4.250e+03	2.826e+00
SSTCOB4 J00095102+6842133	1.1	7	18.560	0.118	5.389e+00	2.644e+03	1.101e-04	2.983e-05	2.665e+03	8.307e-01
SSTCOB4 J00102105+6845167	1.1	5	1.710	3.367	1.841e+00	8.260e+04	1.778e-01	4.992e-04	4.424e+03	8.562e+01
SSTCOB4 J00114782+6847195	1.1	7	4.312	0.990	1.548e+01	8.258e+06	1.758e-02	0.000e+00	4.246e+03	5.611e-01
SSTCOB4 J00115485+6806090	1.1	7	10.140	0.221	4.439e+00	1.407e+05	4.765e-04	7.432e-06	3.123e+03	5.596e-01
SSTCOB4 J00474717+6748538	1.1	5	5.953	0.127	1.238e+00	6.574e+05	1.639e-04	5.343e-08	2.969e+03	1.500e-01
SSTCOB4 J00484602+6803394	1.1	6	13.580	2.034	8.025e+00	8.854e+05	9.935e-05	2.112e-09	4.705e+03	6.410e+00
SSTCOB4 J00465418+6817350	1.1	6	5.689	0.122	1.866e+00	1.296e+05	1.092e-03	9.673e-06	2.892e+03	2.937e-01
SSTCOB4 J00473180+6818507	1.1	6	36.750	3.057	4.580e+00	1.257e+06	3.017e-05	0.000e+00	5.163e+03	1.556e+01

(This table is available in its entirety in machine-readable form.)

is possible that the disagreement can be attributed to differing methodology and insufficient data.

We also followed Panwar et al. (2018) and plotted our YSOs along with PMS isochrones and evolutionary tracks from Siess et al. (2000) and MS isochrones from Girardi et al. (2002) in an optical and a NIR color-magnitude diagram in Figure 18. The NIR CMD is unable to distinguish between the various isochrones, due the isochrones' similarities at dimmer magnitudes and the greater spread in the YSOs' colors at those magnitudes. The optical CMD (while less populated due to the small number of YSOs in our catalog with optical photometry) shows general agreement with an age of 2 Myr for Cep OB4 as reported in Panwar et al. (2018). The evolutionary tracks shown illustrate the diversity of masses and evolutionary stages of our identified YSOs as well as predictions for their future evolution.

7.2. Triggered Star Formation in Cep OB4?

If triggered star formation was a significant process in Cep OB4, ignoring projection effects we would expect to see YSOs generally decreasing in age with increasing distance from the ionizing sources (see Figure 12) in the core of the Be 59 cluster with few sources outside of the bubble. We would expect to find significantly more younger Class I and flat spectrum YSOs in the dense border of the H II region and few to no YSOs beyond the inner edge of the bubble, where the expanding shell has not yet had an effect on the quiescent molecular cloud. Inside the bubble, we would find a large population of Class II and Class III objects.

The distribution of YSOs in Cep OB4 in general follows this expectation, as seen in Figure 19. The Class II and Class III objects are heavily clustered around Be 59 and in the region inside of the bubble. There are many Class I and flat spectrum sources distributed around the edges of the bubble, many at the tips of dense pillars as seen in Figure 13. The exception to this general pattern is the number of Class I and flat spectrum sources near Be 59. However, many of these appear to be associated with the dense reflection nebula to the west of the cluster core and the pillars near Be 59, which the stellar winds and expanding ionized shell has not yet dispersed. Because of the variations in the density of the ISM, and the location relative to the ionizing sources, the relative ages and distribution of young YSOs in Cep OB4 might be more complicated than a simple relation between age and distance from the Be 59 cluster.

To further assess the distribution and evolutionary stages of YSOs beyond the edges of the H II region, we preliminarily ran the *WISE* YSO selections described in Section 4.2 and Appendix C on the entire *WISE* catalog

queried as described in Section 2.3. We identified 169 additional YSOs not found in the selection described in Section 4. All of these YSOs were located around the border or beyond the area covered by the IRAC images. The distribution of the YSO from the catalog compiled in Section 4 and the 169 additional *WISE* YSOs is shown in Figure 19.

From a cursory visual analysis of the distribution, we see that there are numerous young Class I and flat spectrum YSOs just outside of the border and beyond the H II region. The presence of young YSOs – and therefore ongoing or recent star formation – outside of the H II region and beyond the influence of the ionizing shock-wave indicates that there was likely continuing star formation before the creation of the ionized bubble. These objects could also be foreground or background star forming regions not associated with Be 59 and the Cep OB4 cloud. We would have to know the 3-D space location of the YSOs within and outside of the bubble to have a full picture of the star formation sequence in the region. However, the distances to the YSOs are difficult to obtain. They are in general optically faint and undetected by *Gaia* or other parallax observations, and their distance also adds to the difficulty of these measurements.

8. CONCLUSIONS

We have conducted a study of YSOs in the Cep OB4 OB association, using new *Spitzer* IRAC and MMIRS images, publicly available MIPS images, and photometry from 2MASS and *WISE*.

- We extracted 752,615 total unique sources from the IRAC 3.6 and 4.5 μm mosaics. From the limited area mapped by IRAC 5.8 μm 8.0 μm , and MIPS 24 μm , we extracted 2,151, 1,641, and 485 sources respectively with corresponding photometry in IRAC 3.6 or 4.5 μm . We also extracted 113,424 H-band, 114,118 J-band, and 18,369 K-band sources from the MMIRS mosaics that had photometry in IRAC 3.6 or 4.5 μm .
- We cross matched our catalog with photometry from *WISE* and 2MASS, finding 140,594 sources with 2MASS photometry and 126,835 sources with *WISE* photometry.
- We identified 821 YSOs with excess IR emission using a variety of color-color cuts.
- We classified the YSOs based on their IR SED slope α_{IR} and found 67 Class I, 103 flat spectrum sources, 569 Class II, and 82 Class III.
- We identified 5 YSO clusters, 3 located in the Be 59 region and 1 in the region around

IRAS00013+6817. The median cluster size was 11 YSOs and the mean was 103.

- We identified many YSOs located in dense molecular pillars around the edges of the H II region.
- We fit the YSO SEDs with YSO models to estimate their masses and other physical parameters. We constructed the IMF for Cep OB4 and found it to be in general agreement with previous studies.

The distribution of Class I and flat spectrum YSOs is in general consistent with the triggered star formation scenario, but further observations are necessary to confirm that this model describes the sequence of star formation in this region. We plan to propose for Submillimeter Array (Ho et al. 2004) observations to find younger Class 0 and deeply embedded Class I YSOs that are not detected in the IRAC images to locate active sites of star formation in the region. Kinematic data that will allow us to determine the 3D positions and velocities of the stars in the region will help us determine cluster membership and dynamics. We will also perform near-IR spectroscopy on a sample of the YSOs we have detected in order to better determine their masses and ages, which will provide a clearer picture of the star formation activity in Cep OB4.

This work is based on observations made with the *Spitzer* Space Telescope, which was operated by the Jet Propulsion Laboratory, California Institute of Technology under NASA contract 1407. Support for the IRAC instrument was provided by NASA through contract 960541 issued by JPL.

This publication makes use of data products from the Two Micron All Sky Survey, which is a joint project of the University of Massachusetts and the Infrared Processing and Analysis Center/California Institute of Technology, funded by the National Aeronautics and Space Administration and the National Science Foundation.

This publication makes use of data products from the Wide-field Infrared Survey Explorer, which is a joint project of the University of California, Los Angeles, and the Jet Propulsion Laboratory/California Institute of Technology, funded by the National Aeronautics and Space Administration. This research made use of Montage. It is funded by the National Science Foundation under Grant Number ACI-1440620, and was previously funded by the National Aeronautics and Space Administration’s Earth Science Technology Office, Computation Technologies Project, under Cooperative Agreement Number NCC5-626 between NASA and the California Institute of Technology. This research has made use of NASA’s Astrophysics Data System.

The Pan-STARRS1 Surveys (PS1) and the PS1 public science archive have been made possible through contributions by the Institute for Astronomy, the University of Hawaii, the Pan-STARRS Project Office, the Max Planck Society and its participating institutes, the Max Planck Institute for Astronomy, Heidelberg and the Max Planck Institute for Extraterrestrial Physics, Garching, The Johns Hopkins University, Durham University, the University of Edinburgh, the Queen’s University Belfast, the Center for Astrophysics | Harvard & Smithsonian, the Las Cumbres Observatory Global Telescope Network Incorporated, the National Central University of Taiwan, the Space Telescope Science Institute, NASA Grant No. NNX08AR22G issued through the Planetary Science Division of the NASA Science Mission Directorate, the NSF Grant No. AST-1238877, the University of Maryland, Eotvos Lorand University (ELTE), the Los Alamos National Laboratory, and the Gordon and Betty Moore Foundation.

The SAO REU program is funded in part by the National Science Foundation REU and Department of Defense ASSURE programs under NSF Grant no. AST-1852268, and by the Smithsonian Institution.

Facilities: Spitzer (IRAC), WISE

Software: Astropy (Astropy Collaboration et al. 2013, 2018), SAOimageDS9 (Joye & Mandel 2003), Montage (Berriman et al. 2008), SEDFitter (Robitaille et al. 2007)

APPENDIX

A. SOURCE EXTRACTION AND PHOTOMETRY

A.1. IRAC and MIPS Photometry

We performed photometry on the IRAC band 1, 2, 3, and 4 mosaics as well as the MIPS 24 μm image using **Source Extractor** (SExtractor; Bertin & Arnouts 1996). We repeated the source extraction for the short frame mosaics as well in order to obtain accurate magnitudes for the brighter sources. We adjusted the SExtractor parameters to ensure

that most obvious sources were identified while minimizing the number of false detections. The background parameters BACK_SIZE and BACK_FILTERSIZE were the most influential parameters in this process. Setting either to a value much larger than the average source size would neglect variations in background across the image (specifically in regions with significant nebosity). Setting either parameter too small would cause the source flux to be included in the background, potentially preventing their detection. The SExtractor parameters are reported in Table 7 for each of the mosaics.

The zero-point magnitudes were determined for each band using observations of a set of standard stars. For bands 1 and 2 we used standard stars KF06T1, KF06T2, KF08T3, KF09T1, NPM1p60.0581, NPM1p67.0536, and NPM1p68.0422; for bands 3 and 4 we used standard stars NPM1p64.0581, HD165459, NPM1p66.0578, NPM1p67.0536, and NPM1p68.0422. The images of the IRAC calibration stars were obtained by the IRAC calibration program in 2019 January (near in time to the Program 14005 AORs). We produced mosaics of the standard stars using the same methods as used for the Cep OB4 mosaics. For the MIPS calibration, we used calibration stars HD 159330 and HD 173398 whose magnitudes are reported in Engelbracht et al. (2007). SExtractor was run on each standard star using the parameters determined for the Cep OB4 long frame mosaics as described above. The zero-point magnitudes for each band were calculated by minimizing the mean of the difference between the measured magnitudes of the standard stars and their reported calibration magnitudes in Reach et al. (2005) or Engelbracht et al. (2007). After the zero-point magnitudes were determined, we ran SExtractor again on the Cep OB4 mosaics to produce the final calibrated IRAC catalogs and the MIPS catalog. All of the reported IRAC and MIPS magnitudes are calibrated based on Reach et al. (2005) and Engelbracht et al. (2007) respectively, which both base their absolute calibration on Vega.

A.2. MMIRS Photometry

The MMIRS mosaics at each map pointing were extracted separately and the catalogs with calibrated photometry were merged at the end to eliminate duplicate sources where the mosaics overlapped along the edges of each FOV. There was some residual nonlinearity in the extracted photometry, and so the photometry could not be calibrated with a single zero point magnitude. For each image, we cross matched the extracted MMIRS sources to the 2MASS catalog and fit a line to the magnitude difference versus MMIRS magnitude for values with 2MASS magnitudes between 13 and 15 mag. We took the average slope of all images in each band in each set of images (SAO-8-19c and SAO-12-21a) and refit the models using the fixed average slopes but allowing the vertical offset to vary between images. The values of the average slope values are reported with the SExtractor parameters in Table 8. The mosaics were calibrated separately to correct for airmass and to remove the effects of variable sky transmission.

B. 2MASS+IRAC YSO SELECTION

We identified and removed the background sources described in Section 4.1.1 using our IRAC 3.6 and 4.5 μm photometry. We followed the selections described in Winston et al. (2020), which we reformat here for clarity. Objects were considered background sources if they met one of the conditions specified in Equation B1:

$$\begin{aligned}
 & [3.6] < 6.0 \text{ or} \\
 & [4.5] < 5.5 \text{ or} \\
 & ([3.6] > 16.0 \text{ and } [3.6 - 4.5] \geq 1.5) \text{ or} \\
 & ([3.6] > 14.0 \text{ and } [3.6 - 4.5] \leq 0.5) \text{ or} \\
 & ([3.6] > 2([3.6 - 4.5] + 0.5) + 14 \text{ and } [3.6 - 4.5] > 0.5 \text{ and } [3.6 - 4.5] < 1.5)
 \end{aligned} \tag{B1}$$

Our catalog contained 752,615 total sources 711,152 (94%) of which were identified as background sources. This left a remaining 41,463 YSO candidates, 41,059 of which had corresponding 2MASS photometry as determined in Section 3.4. The results of this background source removal are shown in Figure 4.

We then calculated the extinction coefficients A_{K_s} following the method of Flaherty et al. (2007). We only considered the sources with valid values of A_{K_s} , which eliminated 29 sources and reduced the number of YSO candidates to 41,030. We dereddened the photometry for $[K_s - 3.6]$ and $[3.6 - 4.5]$ as follows:

$$\begin{aligned}
 [3.6 - 4.5]_0 &= ([3.6] - A_{3.6} \cdot A_{K_s}) - ([4.5] - A_{4.5} \cdot A_{K_s}) \\
 [K_s - 3.5]_0 &= ([K_s] - A_{K_s}) - ([3.6] - A_{3.6} \cdot A_{K_s})
 \end{aligned} \tag{B2}$$

Where the color excess coefficients are given as $A_J = 2.5$, $A_H = 1.55$, $A_{3.6} = 0.63$, and $A_{4.5} = 0.53$.

We then used three different combinations of 2MASS and IRAC photometry to identify the YSOs from the remaining candidates. We based our selection criteria on that of [Winston et al. \(2020\)](#), but adjusted the criteria in (B4) to better fit our data. We adjusted the selection to be less conservative to account for the smaller amount of scatter in our color-color distribution. In each selection, only sources with valid uncertainty values were used. In the following expressions, we calculate the color uncertainties as $\sigma_{AB}^2 = \sigma_A^2 + \sigma_B^2$.

$$\frac{A_H - A_{4.5}}{A_J - A_H}([J - H] - 0.6 + \sigma_{JH}) + 1.0 + \sigma_{H4.5} < [H - 4.5] \text{ and} \quad (B3)$$

$$[J - H] > 0$$

$$\frac{A_{K_s} - A_{4.5}}{A_H - A_{K_s}}([H - K_s] + \sigma_{HK_s}) + 0.4 + \sigma_{K_s4.5} < [K_s - 4.5] \text{ and} \quad (B4)$$

$$[H - K_s] > 0 \text{ and}$$

$$[K_s - 4.5] > 0.2 + \sigma_{K_s4.5}$$

$$[3.6 - 4.5]_0 - \sigma_{3.6,4.5} > 0 \text{ and}$$

$$[K_s - 3.6]_0 - \sigma_{K_s3.6} > 0.2 \cdot [3.6 - 4.5] + 0.3 \text{ and} \quad (B5)$$

$$[K_s - 3.6]_0 - \sigma_{K_s3.6} > -1.0([3.6 - 4.5]_0 - \sigma_{12}) + 0.8$$

After implementing these selections, we found 388 YSOs using selection (B3), 514 using selection (B4), and 656 using selection (B5) for a total of 719 YSOs identified using the combined 2MASS and IRAC photometry (see Figure 5).

C. WISE YSO SELECTION

Again following the methods of [Winston et al. \(2020\)](#) based on [Fischer et al. \(2016\)](#) and [Koenig & Leisawitz \(2014\)](#), we removed background sources in the subset of our data with *WISE* photometry and identified YSOs from the remaining candidates.

We used the following criteria for identifying background AGN and SFG:

$$\text{SFG} = [W_2 - W_3] > 2.3 \text{ and}$$

$$[W_1 - W_2] < 1.0 \text{ and} \quad (C1)$$

$$[W_1 - W_2] < 0.46([W_2 - W_3] - 0.78) \text{ and}$$

$$[W_1] > 14$$

$$\text{AGN} = [W_1] > 1.8([W_1 - W_3] + 4.1) \text{ and}$$

$$[W_1] > 14 < 1.0 \text{ or} \quad (C2)$$

$$[W_1] > [W_1 - W_3] + 10.0$$

Of the 126,835 sources with *WISE* photometry, 116,796 were identified as AGN and 68,634 as SFG. This left 6,526 remaining *WISE* YSO candidates.

To select the YSOs from the candidates, we used the criteria described in [Fischer et al. \(2016\)](#). Class 1 *WISE* YSOs satisfy:

Class I *WISE* YSOs satisfy all four of the following constraints:

$$W_2 - W_3 > 2.0 \text{ and}$$

$$W_2 - W_3 < 4.5 \text{ and} \quad (C3)$$

$$W_1 - W_2 > 0.46 \cdot (W_2 - W_3) - 0.9 \text{ and}$$

$$W_1 - W_2 > -0.42 \cdot (W_2 - W_3) + 2.2$$

And Class II *WISE* YSO satisfy:

$$\begin{aligned}
 &W_1 - W_2 > 0.25 \text{ and} \\
 &W_1 - W_2 < 0.71 \cdot (W_2 - W_3) - 0.07 \text{ and} \\
 &W_1 - W_2 > -1.5 \cdot (W_2 - W_3) + 2.1 \text{ and} \\
 &W_1 - W_2 > 0.46 \cdot (W_2 - W_3) - 0.9 \text{ and} \\
 &W_1 - W_2 < -0.42 \cdot (W_2 - W_3) + 2.2
 \end{aligned} \tag{C4}$$

Using these selections, we identified 235 total *WISE* YSOs, 52 Class I and 183 Class II (see Figure 6).

D. WISE+IRAC SOURCE SELECTION

The *WISE*+IRAC source selection was performed in exactly the same manner as the selection described in Appendix D, but using IRAC 3.6 and 4.5 μm photometry instead of *WISE* bands 1 and 2. Of the 126,835 sources with *WISE* photometry, 111,879 were identified as AGN and 59,491 as SFG. We also removed 5,625 additional sources that were identified as background sources using 2MASS+IRAC photometry in Appendix B. This left 5,217 remaining *WISE*+IRAC YSO candidates.

We identified 196 total *WISE*+IRAC YSOs, 22 Class I and 174 Class II.

E. MMIRS+IRAC SOURCE SELECTION

The MMIRS+IRAC YSO selections was performed using the same background source removal and selection criteria as in the 2MASS+IRAC selection described in Appendix B. We only included sources with MMIRS photometry below the saturation limit: 12.7 magnitudes for H-band, 12.5 magnitudes for J- band, and 11.1 magnitudes for K-band. We also excluded sources that had corresponding 2MASS photometry above these limits as such sources were saturated and thus had unreliable photometry in the MMIRS images.

After the background source removal, we were left with 10,231 sources with good MMIRS photometry in at least one band, one of which was removed because of a bad extinction coefficient. Notably, due to limited coverage, there were only 1,408 field sources with good K-band MMIRS photometry.

After applying the selections from Appendix B, we found 227 YSOs using selection (B3), 10 using selection (B4), and 3 using selection (B5) for a total of 232 YSOs. This distribution of selection method is due to the very limited K-band MMIRS coverage.

F. IRAC BANDS 3 AND 4 SELECTION

In the regions covered by our IRAC band 3 and/or band 4 mosaics, we removed background sources and selected YSOs following the methods of Winston et al. (2019). We selected 1,166 AGN candidates using the following criteria:

$$\begin{aligned}
 &AGN_1 = [4.5 - 8.0] > 1.2 \text{ and} \\
 &[4.5] > 12.5 + ([4.5 - 8.0] - 4.5)/0.2 \text{ and} \\
 &[4.5] > 12.5
 \end{aligned} \tag{F1}$$

$$\begin{aligned}
 &AGN = AGN_1 \text{ and} \\
 &[4.5] > 15 - 0.5([4.5 - 8.0] - 1) \text{ and} \\
 &([4.5] > 14 + 0.5([4.5 - 8.0] - 2)) \text{ and} \\
 &[4.5] > 15
 \end{aligned} \tag{F2}$$

We selected 1,117 sources that were likely PAH galaxy contaminants satisfying either of the following criteria:

$$\begin{aligned}
 &PAH_1 = [4.5 - 5.8] < (2.5/2)([5.8 - 8.0] - 1) \text{ and} \\
 &[4.5 - 5.8] < 1.55 \text{ and} \\
 &[5.8 - 8.0] > 1 \text{ and} \\
 &[4.5] > 11.5
 \end{aligned} \tag{F3}$$

$$\begin{aligned}
PAH_2 = [3.6 - 5.8] &< (3.2/3)([4.5 - 8.0] - 1) \text{ and} \\
[3.6 - 5.8] &< 2.25 \text{ and} \\
[4.5 - 8.0] &> 1 \text{ and} \\
[4.5] &> 11.5
\end{aligned} \tag{F4}$$

We removed 1 source selected as a knot of possible shocked emission satisfying:

$$\begin{aligned}
KNOT = [3.6 - 4.5] &> 1.05 \text{ and} \\
[3.6 - 4.5] &> (1.2/0.55)([4.5 - 5.8] - 0.3) + 0.8 \text{ and} \\
[4.5 - 5.8] &\leq 0.85
\end{aligned} \tag{F5}$$

We removed 1,234 sources with likely PAH aperture contamination according to the following criteria:

$$\begin{aligned}
PA = [3.6 - 4.5] - \sigma_{12} &\leq 1.5 \cdot ([4.5 - 5.8] - \sigma_{23} - 1) \text{ and} \\
[3.6 - 4.5] - \sigma_{12} &\leq 0.4
\end{aligned} \tag{F6}$$

After removing a combined 2,325 background sources, we were left with 486 candidates for YSO selection with photometry in bands 1 and 2 and either band 3 and/or 4. We calculated extinction coefficients for these sources and removed 5 sources with invalid values.

We selected 45 YSOs using the following four-color IRAC cuts:

$$\begin{aligned}
[5.8 - 8.0] &\geq 0.3 + \sigma_{34} \text{ and} \\
[5.8 - 8.0] &\leq 2 - \sigma_{34} \text{ and} \\
[3.6 - 4.5] &\geq 0.2 + \sigma_{12} \text{ or} \\
[5.8 - 8.0] &\leq 2.5 - \sigma_{34} \text{ and} \\
[3.6 - 4.5] &\geq 0.5 + \sigma_{12} \text{ and} \\
[5.8 - 8.0] &> 2 + \sigma_{34}
\end{aligned} \tag{F7}$$

And 57 using the following additional four-color IRAC cuts:

$$\begin{aligned}
[3.6 - 5.8] &\geq 0.5 + \sigma_{13} \text{ and} \\
[4.5 - 8.0] &\geq 0.5 + \sigma_{24} \text{ and} \\
[3.6 - 4.5] &\geq 0.15 + \sigma_{12} \text{ and} \\
[3.6 - 5.8] + \sigma_{13} &\leq (0.14/0.04) \times ([4.5 - 8.0] - \sigma_{24} - 0.5) + 0.5
\end{aligned} \tag{F8}$$

For the 1,361 sources with detections at 5.8 μm but not 8.0 μm we applied the following cuts to select 8 YSOs:

$$\begin{aligned}
[3.6 - 4.5] - \sigma_{12} &> 0.3 \text{ and} \\
[4.5 - 5.8] - \sigma_{23} &> 0.3
\end{aligned} \tag{F9}$$

We also imposed a final selection for sources with a large color excess, selecting 20 sources:

$$[Ks - 8.0] - \sigma_{k4} > 3 \tag{F10}$$

Altogether, we identified 60 total YSOs through these selections, 9 of which were not identified using the 2MASS+IRAC, *WISE*, *WISE*+IRAC, or MMIRS+IRAC cuts described in Appendices B, C, D, and E.

Table 7. SExtractor parameters for the IRAC long (L) and short (S) and MIPS mosaics

Parameters	3.6 μm L	3.6 μm S	4.5 μm L	4.5 μm S	5.8 μm L	5.8 μm S	8.0 μm L	8.0 μm S	MIPS 24 μm
DETECT_MINAREA (pix)	3	3	3	3	3	3	3	3	3
DETECT_THRESH (σ)	2.25	2.25	2.25	2.25	2.75	2.75	2.50	2.50	2.25
ANALYSIS_THRESH (σ)	2.25	2.25	2.25	2.25	2.75	2.75	2.50	2.50	2.25
DEBLEND_NTHRESH	32	32	32	32	32	32	32	32	32
DEBLEND_MINCOUNT	0.005	0.005	0.005	0.005	0.005	0.005	0.005	0.005	0.005
PHOT_APERTURES (pix)	5	5	5	5	5	5	5	5	5
PHOT_AUTOPARAMS (pix)	2.5, 3.5	2.5, 3.5	2.5, 3.5	2.5, 3.5	2.5, 3.5	2.5, 3.5	2.5, 3.5	2.5, 3.5	2.5, 3.5
MAG_ZEROPOINT	17.68169	17.68169	17.17799	17.17799	16.49360	16.49360	15.47308	15.47308	10.94358
SEEING_FWHM (")	1.6	1.6	1.6	1.6	1.6	1.6	1.6	1.6	1.6
BACK_SIZE (pix)	4	10	4	10	3	3	2	2	2
BACK_FILTERSIZE (pix)	3	7	3	7	3	3	3	3	3

G. MIPS YSO SELECTION

We selected 39 YSOs using the MIPS 24 μm photometry. We removed background sources following the criteria in Appendix F and then followed the methods of [Winston et al. \(2019, 2007\)](#) and [Gutermuth et al. \(2008\)](#) and imposed these selection criteria:

$$\begin{aligned}
 [8.0 - 24] &\geq 1.0 + \sigma_{4m} \text{ and } [5.8 - 8.0] \geq -0.1 - \sigma_{34} \text{ or} \\
 [8.0 - 24] &\geq 0.6 + \sigma_{4m} \text{ and } [5.8 - 8.0] \geq 0.2 - \sigma_{34}
 \end{aligned} \tag{G1}$$

$$\begin{aligned}
 [8.0 - 24] &\geq 1.0 + \sigma_{4m} \text{ and } [3.6 - 4.5] \geq -0.1 - \sigma_{12} \text{ or} \\
 [8.0 - 24] &\geq 0.6 + \sigma_{4m} \text{ and } [3.6 - 4.5] \geq 0.2 - \sigma_{12}
 \end{aligned} \tag{G2}$$

Of the remaining 39 YSOs, 10 were not detected using the 2MASS+IRAC, *WISE*, *WISE*+IRAC, or MMIRS+IRAC cuts described in Appendices B, C, D, and E.

Table 8. SExtractor parameters for the MMIRS mosaics from SAO-8-19c and SAO-12-21a

Parameters	J SAO-8-19c	H SAO-8-19c	K SAO-8-19c	J SAO-12-21a	H SAO-12-21a
DETECT_MINAREA (pix)	3	3	3	3	3
DETECT_THRESH (σ)	2.00	2.00	2.00	2.00	2.00
ANALYSIS_THRESH (σ)	2.00	2.00	2.00	2.00	2.00
DEBLEND_NTHRESH	32	32	32	32	32
DEBLEND_MINCOUNT	0.005	0.005	0.005	0.005	0.005
PHOT_APERTURES (pix)	5	5	5	5	5
PHOT_AUTOPARAMS (pix)	2.5, 3.5	2.5, 3.5	2.5, 3.5	2.5, 3.5	2.5, 3.5
MAG_ZEROPOINT	17.074	17.074	17.074	17.074	17.074
SEEING_FWHM (")	1.6	1.6	1.6	1.6	1.6
BACK_SIZE (pix)	4	4	4	4	4
BACK_FILTERSIZE (pix)	3	3	3	3	3
Average calibration slope	0.033	0.089	0.035	0.035	0.066
Average zero point ^a	23.664	24.431	23.184	24.200	24.398

^a While we ran the source extraction with an arbitrary value for MAG.ZEROPOINT, we calculated the average zero point afterwards by taking the grand mean of the difference in 2MASS and MMIRS magnitudes over all the images in a sample. This value reflects the approximate zero point magnitude for MMIRS without accounting for the nonlinearity.

REFERENCES

- Allen, L. E., Calvet, N., D'Alessio, P., et al. 2004, *ApJS*, 154, 363
- Andre, P., Ward-Thompson, D., & Barsony, M. 2000, *Protostars and Planets IV*, 59
- Astropy Collaboration, Robitaille, T. P., Tollerud, E. J., et al. 2013, *A&A*, 558, A33
- Astropy Collaboration, Price-Whelan, A. M., Sipőcz, B. M., et al. 2018, *AJ*, 156, 123. doi:10.3847/1538-3881/aabc4f
- Berriman, G. B., Good, J. C., Laity, A. C., et al. 2008, *Astronomical Data Analysis Software and Systems XVII*, 83
- Bertin, E., & Arnouts, S. 1996, *A&AS*, 117, 393
- Blanco, V. M., & Williams, A. D. 1959, *ApJ*, 130, 482
- Briceño, C., Preibisch, T., Sherry, W. H., et al. 2007, *Protostars and Planets V*, 345
- Cantat-Gaudin, T., Mapelli, M., Balaguer-Núñez, L., et al. 2019, *A&A*, 621, A115
- Chilini, I., Beletsky, Y., Moran, S., et al. 2015, *PASP*, 127, 406. doi:10.1086/680598
- Elmegreen, B. G., & Lada, C. J. 1977, *ApJ*, 214, 725
- Engelbracht, C. W., Blaylock, M., Su, K. Y. L., et al. 2007, *PASP*, 119, 994
- Fazio, G. G., Hora, J. L., Allen, L. E., et al. 2004, *ApJS*, 154, 10
- Fazio, G. & Megeath, T. 2004, *Spitzer Proposal*, 6
- Fazio, G. & Megeath, T. 2004, *Spitzer Proposal*, 202
- Fischer, W. J., Padgett, D. L., Stapelfeldt, K. L., et al. 2016, *ApJ*, 827, 96
- Flaherty, K. M., Pipher, J. L., Megeath, S. T., et al. 2007, *ApJ*, 663, 1069
- Flewelling, H. A., Magnier, E. A., Chambers, K. C., et al. 2020, *ApJS*, 251, 7. doi:10.3847/1538-4365/abb82d
- Garmany, C. D. 1994, *PASP*, 106, 25
- Getman, K., Feigelson, E., Sicilia-Aguilar, A., et al. 2012, *Spitzer Proposal*, 90179
- Getman, K. V., Broos, P. S., Kuhn, M. A., et al. 2017, *ApJS*, 229, 28
- Girardi, L., Bertelli, G., Bressan, A., et al. 2002, *A&A*, 391, 195. doi:10.1051/0004-6361:20020612
- Gutermuth, R. A., Megeath, S. T., Muzerolle, J., et al. 2004, *ApJS*, 154, 374
- Gutermuth, R. A., Myers, P. C., Megeath, S. T., et al. 2008, *ApJ*, 674, 336
- Gutermuth, R. A., Megeath, S. T., Myers, P. C., et al. 2009, *ApJS*, 184, 18
- Ho, P. T. P., Moran, J. M., & Lo, K. Y. 2004, *ApJL*, 616, L1. doi:10.1086/423245
- Hora, J., Smith, H., Winston, E., et al. 2018, *Spitzer Proposal*, 14005
- Hora, J. L. 2021, *imclean: IRAF Script for interactive corrections to Spitzer/IRAC images*, v3.2, doi:10.5281/zenodo.4850526
- Joncour, I., Duchêne, G., Moraux, E., et al. 2018, *A&A*, 620, A27
- Joye, W. A., & Mandel, E. 2003, *Astronomical Data Analysis Software and Systems XII*, 489
- Kirkpatrick, J. D., Gelino, C., Cushing, M., et al. 2010, *Spitzer Proposal*, 70062
- Kirkpatrick, J. D., Gelino, C., Griffith, R., et al. 2011, *Spitzer Proposal*, 80109
- Koenig, X. P., Allen, L. E., Gutermuth, R. A., et al. 2008, *ApJ*, 688, 1142. doi:10.1086/592322
- Koenig, X. P. & Leisawitz, D. T. 2014, *ApJ*, 791, 131
- Kuhn, M. A., Hillenbrand, L. A., Sills, A., et al. 2019, *ApJ*, 870, 32
- Kun, M., Kiss, Z. T., & Balog, Z. 2008, *Handbook of Star Forming Regions, Volume I*, 136
- Lada, C. J. 1987, *Star Forming Regions*, IAU Symp. 115, 1
- Lada, C. J. 1999, *NATO Advanced Science Institutes (ASI) Series C*, 143
- Lombardi, M. & Alves, J. 2001, *A&A*, 377, 1023. doi:10.1051/0004-6361:20011099
- Loren, R. B. 1976, *ApJ*, 209, 466
- Luisi, M., Anderson, L. D., Schneider, N., et al. 2021, *Science Advances*, 7, eabe9511. doi:10.1126/sciadv.abe9511
- McLeod, B., Fabricant, D., Nystrom, G., et al. 2012, *PASP*, 124, 1318. doi:10.1086/669044
- McKee, C. F. & Ostriker, E. C. 2007, *ARA&A*, 45, 565
- Olano, C. A., Meschin, P. I., & Niemela, V. S. 2006, *MNRAS*, 369, 867
- Ortega, M. E., Paron, S., Giacani, E., et al. 2013, *A&A*, 556, A105
- Ortega, M. E., Paron, S., Areal, M. B., et al. 2020, *A&A*, 633, A27
- Panwar, N., Pandey, A. K., Samal, M. R., et al. 2018, *AJ*, 155, 44
- Patel, N. A., Goldsmith, P. F., Heyer, M. H., et al. 1998, *ApJ*, 507, 241. doi:10.1086/306305
- Reach, W. T., Megeath, S. T., Cohen, M., et al. 2005, *PASP*, 117, 978
- Reipurth, B. 1983, *A&A*, 117, 183
- Rieke, G. H., Young, E. T., Engelbracht, C. W., et al. 2004, *ApJS*, 154, 25
- Robitaille, T.P., Whitney, B. A., Indebetouw, R., et al. 2007, *ApJS*, 169, 328
- Rosvick, J. M. & Majaess, D. 2013, *AJ*, 146, 142

- Schuster, M. T., Marengo, M., & Patten, B. M. 2006, *Proc. SPIE*, 6270, 627020
- Siess, L., Dufour, E., & Forestini, M. 2000, *A&A*, 358, 593
- Skiff, B. A. 2014, *VizieR Online Data Catalog*, B/mk
- Skrutskie, M.F., Cutri R.M., Stiening R., et al. 2006, *AJ*, 131, 1163
- Tiwari, M., Karim, R., Pound, M. W., et al. 2021, *ApJ*, 914, 117. doi:10.3847/1538-4357/abf6ce
- Werner, M. W., Roellig, T. L., Low, F. J., et al. 2004, *ApJS*, 153, 1
- Winston, E., Megeath, S. T., Wolk, S. J., et al. 2007, *ApJ*, 669, 493
- Winston, E., Hora, J., Gutermuth, R., et al. 2019, *ApJ*, 880, 9
- Winston, E., Hora, J. L., & Tolls, V. 2020, *AJ*, 160, 68. doi:10.3847/1538-3881/ab99c8
- Wright E. L., Eisenhardt, P. R. M., Mainzer, A. K., et al. 2010, *AJ*, 140, 868
- Xu, X., Ester, M., Kriegel, H.-P., et al. 1997, *Vistas in Astronomy*, 41, 397
- Xu, J.-L., Wang, J.-J., Ning, C.-C., et al. 2014, *Research in Astronomy and Astrophysics*, 14, 47-65
- Zinnecker, H., & Yorke, H. W. 2007, *ARA&A*, 45, 481